Combined heat and mass transfer analyses in catalytic microreactors partially filled with porous material- The influences of nanofluid and different porous-fluid interface models

David G.P. Guthrie [a], Mohsen Torabi [1,b], Nader Karimi [1,a,c]

[a] School of Engineering, University of Glasgow, Glasgow G12 8QQ, United Kingdom

[b] School of Engineering, University of California, Merced, CA 95343, USA

[c] Civil and Mechanical Engineering Department, University of Missouri-Kansas City, Kansas City, MO 64110, USA

Abstract

This paper reports a theoretical analysis of heat and mass transfer in the microchannels partially filled with porous materials and used in thermos-chemical microreactors. A first order catalytic chemical reaction is considered on the internal surfaces of a parallel-plates microchannel. The local thermal non-equilibrium approach along with two well-established porous-fluid interface models is employed to investigate the heat transfer within the porous section of the microreactor. The analysis further accounts for the finite thickness of the surrounding solid walls of the microchannel. The dispersion equations in both porous and clear sections of the microchannel are coupled with the fluid temperature through considering the thermal diffusion of mass. In addition, to enhance heat transfer in the partially-filled microchannel, the base fluid is replaced by a nanofluid. The results show that inclusion of the finite thickness of the walls in the thermal analysis can majorly affect the temperature fields and Nusselt number (*Nu*). In particular, the optimal thickness of the porous insert for achieving the maximum *Nu* is found to be strongly influenced by the wall thickness. It is also shown that the specific porous-fluid interface model, thicknesses of the porous section and that of the walls, and the volumetric concentration of the nanoparticles can all impart significant effects upon the concentration of chemical species and their distribution across the microchannel. More specifically, the concentration field within the porous region is found to be considerably dependent on the implemented porous-fluid interface model.

Keywords: Heat and mass transfer; Microreactor; Forced convection; Soret number; Local thermal non-equilibrium; Double-diffusive.

[1] Corresponding authors.
E-mails: Mohsen.Torabi@my.cityu.edu. hk (M. Torabi), Nader.Karimi@glasgow.ac.uk (N.Karimi).

Nomenclature

a_{sf}	interfacial area per unit volume of porous media, m^{-1}	S_{nf}	Volumetric internal heat generation rate for the nanofluid phase, $W.m^{-3}$
Bi	Biot number	Sr_1, Sr_2	Soret Number
C_0	Reference concentration, $Kg.m^{-3}$	T_1	Temperature of the walls, K
C_1, C_2	Concentration of the chemical products per unit volume, $Kg.m^{-3}$	T_{nf_1}, T_{nf_2}	Temperature of the nanofluid, K
$c_{p,nf}$	Specific heat of the fluid phase of the porous medium, $J.kg^{-1}.K^{-1}$	T_s	Temperature of the solid phase of the porous medium, K
D_1, D_2	Diffusion coefficient, $m^2.s^{-1}$	$\overline{U}$	Average dimensionless velocity
Da	Darcy number	u_p	Velocity of the nanofluid in porous medium, $m.s^{-1}$
D_{T_1}, D_{T_2}	Thermodiffusion coefficient,$m^2.s^{-1}.K^{-1}$	U_p, U_{nf}	Dimensionless velocity
h_1	Half-thickness of the microchannel, m	Y_0	Dimensionless height of the inner boundary of the upper wall
h_0	Height of the inner boundary of the upper wall, m	Y_p	Dimensionless half-thickness of the porous insert
h_p	Half-thickness of the porous insert, m	***Greek symbols***	
h_{sf}	Internal heat convection coefficient, $W.m^{-2}.K^{-1}$	λ	Damköhler number
k	Solid to fluid effective thermal conductivity ratio	ϵ	Porosity
k_1	Thermal conductivity of solid walls, $W.m^{-1}.K^{-1}$	θ_1	Dimensionless temperature of the solid walls
k_{1s}	Ratio of the porous solid phase to solid wall thermal conductivities	$\theta_{nf_1}, \theta_{nf_2}$	Dimensionless temperature of the nanofluid phase
$k_{e,f}$	Effective thermal conductivity of the fluid phase of the porous medium, $W.m^{-1}.K^{-1}$	θ_m	Dimensionless average temperature of the nanofluid phase
$k_{e,s}$	Effective thermal conductivity of the solid phase of the porous medium, $W.m^{-1}.K^{-1}$	θ_s	Dimensionless temperature of the solid phase of the porous medium
k_f	Thermal conductivity of the base fluid, $W.m^{-1}.K^{-1}$	κ	Permeability, m^2

k_{nf}	Thermal conductivity of the nanofluid, W. m^{-1}. K^{-1}	$\mu_{e,nf}$	Dynamic viscosity of porous medium, Kg. s^{-1}. m^{-1}
k_p	Thermal conductivity of the nanoparticles, W. m^{-1}. K^{-1}	μ_f	Dynamic viscosity of the base fluid, Kg. s^{-1}. m^{-1}
k_d	Reaction kinetic constant, m. s^{-1}	μ_{nf}	Dynamic viscosity of the nanofluid, Kg. s^{-1}. m^{-1}
Nu	Nusselt Number	ω_s	Dimensionless volumetric internal heat generation rate for the solid phase of the porous medium
p	Pressure, Pa	ω_{nf}	Dimensionless volumetric internal heat generation rate for the nanofluid phase
Q_1	Dimensionless volumetric internal heat generation rate for the solid walls	ρ_{nf}	density of the nanofluid phase,kg. m^{-3}
q_1	Volumetric internal heat generation rate for the solid wall, W. m^{-3}	Φ_1, Φ_2	Dimensionless concentration
S_s	Volumetric internal heat generation rate for the solid phase of the porous medium, W. m^{-3}		

1. Introduction

Recent advancements in manufacturing techniques have provided a great opportunity to minimize the scale of various systems. Hence, energy-related devices have been continuously shrinking during the recent past years [1][2]. The two important reasons behind miniaturization of these devices are i) less energy consumption and hence easier to find energy sources for portable devices and ii) lower volume, which ultimately means transportation and shipping cost reduction [2]. Accordingly, microreactors have recently gained considerable attention [3][4]. Use of microreactors, in lieu of conventional chemical reactors, in thermochemical systems offers various advantages such as smaller volume, higher surface-to-volume ratio, less material cost, safer reactions, and higher quality of the products to name a few [5]. Hence, they continue to grow in various industrial and scientific fields, including high throughput screening in microanalytical chemistry [6], reaction kinetics and mechanisms studies [7], and fast reactions [8]. Most importantly, thermochemical microreactors are now used for production of hydrogen and renewable fuels [1][9].

The fluid flow and heat transfer analyses of microchannels, which are the building blocks of microreactors, have been the focus of many investigations [10]. Some modifications need to be made on the design and modelling of a microchannel when used as an elementary unit of a microreactor. In practical microreactors the wall thickness and the height of the microchannel are very much comparable [11]. Thus, walls' thicknesses should be included in the design and analyses. Moreover, a microchannel as a part of microreactor, can be filled with a porous material leading to the enhancement of the mixing process and/or catalytic reactions [12][13]. While local thermal equilibrium (LTE) approach has been extensively used to analyse the heat transfer aspect of porous structures, recently local thermal non-equilibrium (LTNE) approach has overtaken LTE for small scales [14]. In LTE method one mean temperature is considered for both solid and fluid phases of the porous section of the system. However, LTNE approach recognises the temperature difference between the solid and fluid phases of the porous medium, and correlates them via a heat transfer coefficient which couples energy equations of the solid and fluid phases of the porous material [15]. Although using LTNE method is more costly compared with LTE, it is more reliable and provides more accurate results prediction of the temperature fields inside the system [16]. Most importantly, it has been recently shown that the results of this approach are superior to those of LTE, particularly in the presence of heat generating/consuming chemical reactions [10][17]. This superiority also improves the mass transfer analysis when the dispersion and energy equations of the fluid phase are coupled by the thermal diffusion of mass [18][19]. Nonetheless, recent studies have shown that the LTNE analyses of porous channels are highly sensitive to the choice of porous interface model, and thus it is important to repeat the analysis under different interface models [20][32][20]. It should be, however, noted that comparable thermal conductivities of the solid and fluid phases of the porous medium, and similar heat generation/consumption in these phases result in comparable temperatures in the two phases. Thus, under these conditions the LTNE and LTE models converge and using LTE model within the porous medium of the system would give enough accuracy [21].

Consideration of thick walls and porous inserts have been the focus of recent studies on microreactors [22][23]. However, all previous studies have been performed for either non-porous microreactors or fully-filled porous microreactors. To increase the flow rate or decrease the pumping cost in a porous channel, partial filling of the channel with porous material is an effective method [24][25]. At the same time, it offers the advantages of porous structure in the system such as enhancing Nusselt number (Nu) and mixing [26].

A few points follow from the preceding review of literature. First, the general problem of partially filled porous channels and microchannels have already received significant attention, see for example [17][25][26][27]. As an essential commonality, all these investigations ignore the existence of the channel walls. Yet, there is now a growing body of evidence indicating that the finite thickness of the wall can significantly affect the thermal behaviour of microchannels [28][29][30]. Second, in general accurate calculation of the temperature is central to performance prediction of thermochemical microreactor [31][1]. Further, it is now well-demonstrated that exothermic and endothermic reactions can invalidate the LTE approach in porous microreactor [17][27]. Nonetheless, the bulk of existing theoretical and numerical studies have taken an LTE approach, e.g. [18][19]. Third, given the existence of sharp temperature gradients in thermochemical microreactors, thermal diffusion of mass is of significance, although this has been ignored in most investigation. The problem of microchannels and microreactors with relatively similar geometries have been considered in our previous investigations [24][17][32][20]. However, microreactors with thick walls, partially filled with porous materials and including surface reactions have remained unexplored. The proceeding analysis shows that consideration of LTNE in such configuration can highly affect the mass transfer process.

The current work aims to address these issues through a theoretical analysis of a catalytic microreactor. The present investigation provides an insight into the effects of partial porous filling on the transport of heat and mass in thick-wall microreactors. In particular, the influences of different porous-fluid interface models upon the transport processes are analysed in detail.

2. Theoretical methods

2.1. Problem configuration and assumptions

Microreactors usually consist of a series of microchannels partially filled with a porous insert, through which fluid can flow. The thermal conductivity of the fluid may be augmented with nanoparticles, and microreactor can feature internal heat generation or consumption with either physical or chemical natures [33][34][35]. The schematic view in Fig. 1 presents this arrangement. Within the microchannel there are a clear region, through which fluid can flow freely and a strip of porous material, inserted along the centreline. The thickness of the walls of the microchannel are taken into account and the external surface of each wall is subjected to a constant heat flux. The microchannel is deep enough about the z-axis, so that its 2D x-y planar model would be an accurate representation. Also, it is axisymmetric about y-axis and therefore only half of the configuration is investigated. The parameter h_p represents the distance from the

centreline to the edge of the porous insert, h_0 the distance to the inner surface of the wall, and h_1 the distance to the boundary of the configuration. The subsequent analysis relies on the following assumptions:

- The porous material is homogeneous and isotropic and under local thermal non-equilibrium.
- It is assumed that the flow on the microscopic scale within the porous microreactor is stokes flow and the microscale Reynolds number is negligible. Thus, the Darcy model for the porous media governs the momentum equation of the system [36].
- The flow is incompressible, steady and laminar, and is both thermally and hydrodynamically fully developed throughout the entire length of the microchannel.
- The nanoparticles are distributed uniformly and the species mass transfer Peclet number is assumed to be small.
- Internal heat generations occur uniformly in all components of the system according to the provided rates. This could be due to homogeneous chemical reactions, dissipation of electrical energy or absorption of electromagnetic waves.
- All thermophysical properties of the system (i.e. porosity, density, thermal conductivity, nanoparticle concentration and specific heat) are invariant with respect to both temperature and concentration.
- Thermal radiation and natural convection are ignored.
- A first order chemical reaction occurs at the internal surfaces of the system walls, wherein chemical species are consumed [19][37]. The transportation of such species occurs through the mechanisms of Fickian and thermal diffusion of chemical species [38][39].

2.2. Governing equations

Considering the assumptions stated in Section 2.1, the governing equations of the problem are as follows. The momentum equation in the clear flow region reduces to:

$$-\frac{\partial p}{\partial x}+\mu_{nf}\frac{\partial^2 u_f}{\partial y^2}=0 \ \text{ for } \ h_p<y<h_0. \tag{1}$$

For the transport of momentum in the porous region of the microchannel, the Darcy-Brinkman flow model is utilised, which reads

$$-\frac{\partial p}{\partial x}+\mu_{e,nf}\frac{\partial^2 u_p}{\partial y^2}-\frac{\mu_{nf}}{K}u_p=0 \ \text{ for } \ 0<y<h_p. \tag{2}$$

where $\mu_{e,nf} = \frac{\mu_{nf}}{\epsilon}$. The following equations describe the transport of thermal energy throughout each of the system's components. They correspond, respectively, to the wall, the clear region, and the nanofluid and solid phases of the porous region [40][25]:

$$k_1 \frac{d^2 T_1}{dy^2} + q_1 = 0 \text{ for } h_0 < y < h_1, \tag{3}$$

$$\rho_{nf} c_{nf,p} u_{nf} \frac{\partial T_{nf1}}{\partial x} = k_{nf} \frac{\partial^2 T_{nf1}}{\partial y^2} + S_{nf} \text{ for } h_p < y < h_0, \tag{4}$$

$$\rho_{nf} c_{nf,p} u_p \frac{\partial T_{nf2}}{\partial x} = k_{e,nf} \frac{\partial^2 T_{nf2}}{\partial y^2} + a_{sf} h_{sf} \left(T_s - T_{nf2}\right) + S_{nf} \text{ for } 0 < y < h_p, \tag{5}$$

$$0 = k_{e,s} \frac{\partial^2 T_s}{\partial y^2} - a_{sf} h_{sf} \left(T_s - T_{nf2}\right) + S_s \text{ for } 0 < y < h_p. \tag{6}$$

The above equations are, respectively, govern the transport of energy in the solid wall, nanofluid in the open space, and nanofluid and solid phases of the porous section of the microreactor. Moreover, Eq. (3) assumes an internal heat generation within the solid walls of the microreactor. This, for instance, can be the result of absorption of microwave in the solid walls [41][42]. Considering the Fickian diffusion of species and contributions of the Soret effect, the dispersion equations for both sections of the microchannel are given as follows [39]:

$$D_1 \frac{\partial^2 C_1}{\partial y^2} + D_{T_1} \frac{\partial^2 T_{nf1}}{\partial y^2} = 0 \text{ for } h_p < y < h_0, \tag{7}$$

$$D_2 \frac{\partial^2 C_2}{\partial y^2} + D_{T_2} \frac{\partial^2 T_{nf2}}{\partial y^2} = 0 \text{ for } 0 < y < h_p. \tag{8}$$

It is noted that the values of D_{T_1} and D_{T_2} can be either positive or negative [28] and thus the thermal diffusion term can be also subtracted from the Fickian diffusion term.

It is worth noting that the momentum, energy and dispersion governing equations of the problem can be written in vector form, and hence simplified to three set of equations [43][44]. However, to keep with the previous studies [23][32][22], and make it easier for the readers to follow the analytical procedure, expanded formats of the governing equations have been given.

2.3. Boundary equations

The boundary conditions applied to the momentum equations are as follows.

$$\frac{\partial u_p}{\partial y} = 0 \text{ at } y = 0, \tag{9a}$$

$$u_{nf} = u_p, \quad \mu_{nf}\frac{\partial u_{nf}}{\partial y} = \mu_{e,nf}\frac{\partial u_p}{\partial y} \text{ at } y = h_p, \tag{9b}$$

$$u_{nf} = 0 \text{ at } y = h_0. \tag{9c}$$

Those related to the energy equations are:

$$\frac{\partial T_{nf2}}{\partial y} = \frac{\partial T_s}{\partial y} = 0 \text{ at } y = 0, \tag{10a}$$

$$T_{nf1} = T_{nf2} \text{ at } y = h_p, \tag{10b}$$

$$T_1 = T_{nf1}, \qquad k_{nf}\frac{\partial T_{nf1}}{\partial y} = k_1\frac{\partial T_1}{\partial y} = q|_{y=h_0} \text{ at } y = h_0, \tag{10c}$$

$$k_1\frac{\partial T_1}{\partial y} = q_w \text{ at } y = h_1, \tag{10d}$$

while the boundary conditions for the dispersion equations are given by:

$$\frac{\partial C_2}{\partial y} = 0 \text{ at } y = 0, \tag{11a}$$

$$C_1 = C_2, \qquad D_1\frac{\partial C_1}{\partial y} = D_2\frac{\partial C_2}{\partial y} \text{ at } y = h_p, \tag{11b}$$

$$D_1\frac{\partial C_1}{\partial y} = k_d C_1 \text{ at } y = h_0. \tag{11c}$$

There are two well-established models that describe the heat flux over a porous-fluid interface: Models 1A and 2A of Alazmi and Vafai [45], or models A and B of Yang and Vafai [46]. According to Model A, the total heat flux at the interface of the porous insert is the sum of heat fluxes of the individual phases; defined by their effective thermal conductivities and temperature gradient, respectively. That is

$$q_{int} = k_{e,nf}\frac{\partial T_{nf2}}{\partial y}\bigg|_{y=h_p} + k_{e,s}\frac{\partial T_s}{\partial y}\bigg|_{y=h_p} = k_{nf}\frac{\partial T_{nf1}}{\partial y}\bigg|_{y=h_p} \text{ at } y = h_p, \tag{12a}$$

$$T_{nf1} = T_{nf2} = T_s \text{ at } y = h_p. \tag{12b}$$

Alternatively, Model B assumes that both solid and fluid phases receive equal heat flux at the interface:

$$q_{int} = k_{e,nf}\frac{\partial T_{nf2}}{\partial y}\bigg|_{y=h_p} = k_{e,s}\frac{\partial T_s}{\partial y}\bigg|_{y=h_p} = k_{nf}\frac{\partial T_{nf1}}{\partial y}\bigg|_{y=h_p} \text{ at } y = h_p. \tag{13}$$

Taking the average fluid velocity for the entire microchannel, defined as

$$\overline{u} = \frac{1}{h_0}\left[\int_0^{h_p} u_p dy + \int_{h_p}^{h_0} u_f dy\right], \tag{14}$$

and recalling that for a fully developed flow, incorporating the assumptions stated in Section 2.1, $\frac{\partial T_{nf1}}{\partial x} = \frac{\partial T_{nf2}}{\partial x} = \frac{\partial T_s}{\partial x} = \frac{\partial T_1}{\partial x} = \frac{\partial T}{\partial x}$, the following derivations can be carried out. Firstly, Eq. (3) can be integrated from h_0 to h_1 to yield

$$q_w - q|_{y=h_0} + q_1(h_1 - h_0) = 0. \tag{15}$$

Similarly, Eq. (4) can be integrated from h_p to h_0:

$$\rho_{nf} c_{nf,p} \frac{\partial T}{\partial x} \int_{h_p}^{h_0} u_{nf} dy = q|_{y=h_0} - q|_{y=h_p} + S_{nf}(h_0 - h_p). \tag{16}$$

Combining Eqs. (5) and (6) gives,

$$\rho_{nf} c_{nf,p} u_p \frac{\partial T}{\partial x} = k_{e,s} \frac{\partial^2 T_s}{\partial y^2} + k_{e,nf} \frac{\partial^2 T_{nf2}}{\partial y^2} + S_s + S_{nf,} \tag{17}$$

and integrating the result over the porous region, while applying Eq. (12), the Model A boundary condition provides

$$\rho_{nf} c_{nf,p} \frac{\partial T}{\partial x} \int_0^{h_p} u_p dy = q|_{y=h_p} + h_p(S_s + S_{nf}). \tag{18}$$

Combining Eqs. (15), (16) and (18), and using Eq. (14) reveals

$$\rho_{nf} c_{nf,p} \frac{\partial T}{\partial x} = \frac{q_w}{h_0 \overline{u}} + \frac{q_1(h_1 - h_0)}{h_0 \overline{u}} + \frac{S_{nf} h_0 + S_s h_p}{h_0 \overline{u}}, \tag{19}$$

and by means of substituting Eq. (19) into Eq. (18), a prediction of the heat flux at the porous-fluid interface under model A conditions can be derived as

$$\begin{aligned} \left.\frac{q|_{y=h_p}}{q_w}\right|_{Model\ A} &= \frac{1}{h_o \overline{u}} \int_0^{h_p} u_p dy \\ &+ \frac{1}{q_w}\left[\frac{1}{h_o \overline{u}}\left(q_1(h_1 - h_0)\int_0^{h_p} u_p dy + (S_{nf} h_0 + S_s h_p)\int_0^{h_p} u_p dy\right) - h_p(S_s \right. \\ &\left. + S_{nf})\right]. \end{aligned} \tag{20}$$

Similarly, integrating Eq. (17) over the porous region and applying Eq. (13), model B boundary condition, yields

$$\rho_{nf} c_{nf,p} \frac{\partial T}{\partial x} \int_0^{h_p} u_p dy = 2q|_{y=h_p} + h_p(S_s + S_{nf}), \tag{21}$$

and combining Eqs. (15), (16) and (21) renders

$$\rho_{nf} c_{nf,p} \frac{\partial T}{\partial x} = \frac{q_w}{h_0 \overline{u}} + \frac{q|_{y=h_p}}{h_0 \overline{u}} + \frac{q_1(h_1 - h_0)}{h_0 \overline{u}} + \frac{S_{nf} h_0 + S_s h_p}{h_0 \overline{u}}, \tag{22}$$

which, through substitution into Eq. (21), provides the model B prediction of the heat flux at the porous-fluid interface. This reads,

$$\left.\frac{q|_{y=h_p}}{q_w}\right|_{Model\ B} = \frac{\int_0^{h_p} u_p dy}{2h_0\overline{u}-\int_0^{h_p} u_p dy} + \frac{1}{2h_0\overline{u}-\int_0^{h_p} u_p dy}\left[\frac{1}{q_w}\left(h_p\left(S_s+S_{nf}\right) - \frac{\int_0^{h_p} u_p dy}{h_o\overline{u}}\left(q_1(h_1-h_0) + S_{nf}h_0 + S_s h_p\right)\right)\right]. \tag{23}$$

Lastly, by rearranging the terms in Eq. (15), an expression for the heat flux at the fluid-wall interface is developed, valid for both Models A and B:

$$\frac{q|_{y=h_0}}{q_w} = 1 + \frac{q_1(h_1-h_0)}{q_w}. \tag{24}$$

2.4. Normalisations and velocity profiles

In order to normalise the previously discussed governing equations and boundary conditions, the following dimensionless variables are introduced,

$$\theta|_{Model\ A} = \frac{k_{e,s}(T-T_{int})}{q_w h_1}, \qquad \theta|_{Model\ B} = \frac{k_{e,s}\left(T-T_{s,int}\right)}{q_w h_1}, \qquad \gamma_p = \frac{q|_{y=h_p}}{q_w},$$

$$\gamma_s = \frac{q|_{y=h_0}}{q_w}, \qquad k = \frac{k_{e,s}}{k_{e,f}}, \qquad k_{1s} = \frac{k_1}{k_{e,s}},$$

$$Bi = \frac{a_{sf}h_{sf}h_0^2}{k_{e,s}}, \qquad Y = \frac{y}{h_1}, \qquad Y_p = \frac{h_p}{h_1},$$

$$Y_0 = \frac{h_0}{h_1}, \qquad U = \frac{u}{u_r}, \qquad Q_1 = \frac{q_1 h_1}{q_w},$$

$$\omega_{nf} = \frac{S_{nf}h_1}{q_w}, \qquad \omega_s = \frac{S_s h_1}{q_w}, \qquad Da = \frac{\kappa}{h_1^2}, \tag{25}$$

$$D_{21} = \frac{D_2}{D_1}, \qquad \lambda = \frac{k_d h_1}{D_1}, \qquad Sr_1 = \frac{D_{T_1} q_w h_1}{D_1 C_0 k_{e,s}},$$

$$Sr_2 = \frac{D_{T_2} q_w h_1}{D_2 C_0 k_{e,s}}, \qquad \Phi_1 = \frac{C_1}{C_0}, \qquad \Phi_2 = \frac{C_2}{C_0},$$

$$C_k = \frac{k_{nf}}{k_f} = 1 + \frac{3\phi(\frac{k_p}{k_f}-1)}{(\frac{k_p}{k_f}+2)-\phi(\frac{k_p}{k_f}-1)}, \qquad C_\mu = \frac{\mu_{nf}}{\mu_f} = \frac{1}{1-\phi^{2.5}}.$$

Darcy number Da describes the permeability of the porous medium relative to the size of the microchannel, while Biot number (Bi) represents the strength of the internal heat exchange between fluid and solid phases in the porous region. Soret number (Sr) describes the relationship between the

temperature gradient inside the system and the concentration flux of chemical species in the flow; while the Damköhler number λ relates the chemical reaction rate to the rate of mass diffusion in the system. The nanofluid property ratios C_k and C_μ indicate the relationship between the base fluid and the equivalent nanofluid, in terms of thermal conductivity and viscosity, respectively [24]. The mathematical models used to represent these ratios were developed by Maxwell-Garnetts and Brinkman and are widely used in the theoretical modelling of nanofluids, see for example [47][48]. The characteristic velocity of the flow u_r is defined as $u_r = -\frac{h_0^2}{\mu_e}\frac{\partial P}{\partial x}$.

2.5. Solid and fluid temperature fields

By using dimensionless parameters given in Eq. (25) and incorporating boundary conditions related to each model, the set of momentum, energy and dispersion equations is redefined. Some algebraic manipulations reveal the following temperature distributions for each scenario. The detailed procedure has been provided in Appendix A.

2.5.1. Model A prediction of the temperature fields

By solving non-dimensionalized decoupled energy equations for Model A and applying relevant boundary conditions, the temperature fields across the microchannel can be obtained. Firstly, for the solid wall:

$$\theta_1(Y) = -\frac{Q_1 Y^2}{2k_{1s}} + A_1 + A_2 Y, \tag{26}$$

and the temperature field for the clear region is given by

$$\theta_{nf1}(Y) = Y^3 b\frac{k\varepsilon\chi_A}{6C_k\overline{U}Y_0} - Y^4\frac{k\varepsilon\chi_A}{24C_kC_\mu\overline{U}Y_0} + Y^2\left(-\frac{k\omega_{nf}\varepsilon}{2C_k} + a\frac{k\varepsilon\chi_A}{2C_k\overline{U}Y_0}\right) + A_3 + A_4 Y. \tag{27}$$

Further, the temperature fields for the nanofluid and solid phases of the porous region are respectively resolved to the following forms,

$$\theta_{nf2}(Y) = -\frac{kY^2\left(C_\mu\overline{U}\omega_s + C_\mu\overline{U}\omega_{nf}Y_0 - DaY_0\chi_A\right)}{2C_\mu\overline{U}(k + C_kY_0)} + A_5\frac{C_kY_0^2}{Bi(k + C_kY_0)}\cosh(\alpha Y) + A_6 + c\frac{k(-Bi + Y_0Z^2)\chi_A}{\overline{U}Z^2(-kBi - BiC_kY_0 + C_kY_0^2Z^2)}\cosh(ZY), \tag{28}$$

$$\theta_s(Y) = -\frac{kY^2\left(C_\mu\overline{U}\omega_s + C_\mu\overline{U}\omega_{nf}Y_0 - DaY_0\chi_A\right)}{2C_\mu\overline{U}(k + C_kY_0)} + A_7\frac{C_kY_0^2}{Bi(k + C_kY_0)}\cosh(\alpha Y) + A_8 + c\frac{kBi\chi_A}{\overline{U}Z^2(kBi + BiC_kY_0 - C_kY_0^2Z^2)}\cosh(ZY), \tag{29}$$

where $\chi_A = (1 + Q_1(1 - Y_0) + \omega_{nf}Y_0 + \omega_s Y_p)$, $\alpha = \frac{\sqrt{Bi}\sqrt{k+C_k Y_0}}{\sqrt{C_k}Y_0}$ and constants a, b and c are provided in Appendix A.

2.5.2. Model B predictions of the temperature fields

By solving the non-dimensionalized energy equation ODEs related to Model B and suitable boundary conditions, a full representation of the temperature field at each point across the system is established. For the solid wall:

$$\theta_1(Y) = -\frac{Q_1 Y^2}{2k_{1s}} + B_1 + B_2 Y, \tag{30}$$

and for the nanofluid in the clear region:

$$\theta_{nf1}(Y) = Y^3 b\frac{k\varepsilon\chi_B}{6C_k\overline{U}Y_0} - Y^4\frac{k\varepsilon\chi_B}{24C_kC_\mu\overline{U}Y_0} + Y^2\left(-\frac{k\omega_{nf}\varepsilon}{2C_k} + a\frac{k\varepsilon\chi_B}{2C_k\overline{U}Y_0}\right) + B_3 + B_4 Y. \tag{31}$$

The temperature fields of the nanofluid and solid phases of the porous region are given by

$$\begin{aligned}\theta_{nf2}(Y) = &-\frac{kY^2\left(C_\mu\overline{U}\omega_s + C_\mu\overline{U}\omega_{nf}Y_0 - DaY_0\chi_B\right)}{2C_\mu\overline{U}(k + C_kY_0)} + B_5\frac{C_kY_0^2}{Bi(k + C_kY_0)}\cosh(\alpha Y) + B_6\\ &+ c\frac{k(-Bi + Y_0Z^2)\chi_B}{\overline{U}Z^2(-kBi - BiC_kY_0 + C_kY_0^2Z^2)}\cosh(ZY),\end{aligned} \tag{32}$$

$$\begin{aligned}\theta_s(Y) = &-\frac{kY^2\left(C_\mu\overline{U}\omega_s + C_\mu\overline{U}\omega_{nf}Y_0 - DaY_0\chi_B\right)}{2C_\mu\overline{U}(k + C_kY_0)} + B_7\frac{C_kY_0^2}{Bi(k + C_kY_0)}\cosh(\alpha Y) + B_8\\ &+ c\frac{kBi\chi_B}{\overline{U}Z^2(kBi + BiC_kY_0 - C_kY_0^2Z^2)}\cosh(ZY),\end{aligned} \tag{33}$$

where $\chi_B = (1 + \gamma_p|_{Model\ B} + Q_1(1 - Y_0) + \omega_{nf}Y_0 + \omega_s Y_p)$, $\alpha = \frac{\sqrt{Bi}\sqrt{k+C_kY_0}}{\sqrt{C_k}Y_0}$ and constants a, b and c are provided in Appendix A.

2.5.3. LTE solution

Adding the two energy equations in the porous section of the microchannel results in the LTE temperature field. This reads,

$$\theta_{LTE}(Y) = C_{LTE} + \frac{k\left(-\frac{1}{2}C_\mu\overline{U}Y^2\left(\omega_{nf}Y_0 + \omega_s\right) + \chi\left[\frac{1}{2}DaY_0Y^2 + \frac{c}{Z^2}C_\mu\cosh(ZY)\right]\right)}{C_\mu\overline{U}\left(k + C_\mu Y_0\right)}, \tag{34}$$

where $\chi = (1 + Q_1(1 - Y_0) + \omega_{nf}Y_0 + \omega_s Y_p)$ and coefficient C_{LTE} consists of lengthy long-form algebra not provided here.

2.6. Nusselt Number

The Nu at the inside of the microchannel wall for the partial-filling conditions and fully developed flow, where $Y_p < Y_0$, can be found by referring to Rohsenow et al. [49]:

$$Nu = \frac{q|_{y=h_0} D_h}{k_{e,nf}(T|_{y=h_0} - T_m)}, \tag{35}$$

where D_h is the hydraulic diameter of the microchannel and equates to $4h_0$. Normalisation of Eq. (35), using the dimensionless parameters defined by Eq. (25), results in

$$Nu = \frac{4\varepsilon k \gamma_s}{\theta_w - \theta_m} \text{ for } Y_p < Y_0, \tag{36}$$

$$Nu = \frac{4\varepsilon \gamma_s}{\theta_w - \theta_m} \text{ for } Y_p = Y_0. \tag{37}$$

where $\theta_w = \theta_{nf1}|_{Y=Y_0}$ and θ_m represent the mean temperature in the microchannel, defined as:

$$\theta_m = \frac{\int_0^{Y_p} U_p \theta_{nf2} dy + \int_{Y_p}^{Y_0} U_{nf} \theta_{nf1} dy}{\overline{U}}. \tag{38}$$

2.6. Mass transfer and concentration profiles

Returning to the normalised quantities provided in Eq. (25), dimensionless versions of Eqs. (7) and (8) can be derived. The transport of mass within the system is therefore given by

$$\Phi_1'' + Sr_1 \theta_{nf1}'' = 0 \text{ for } Y_p < Y < Y_0, \tag{39}$$

$$\Phi_2'' + Sr_2 \theta_{nf2}'' = 0 \text{ for } 0 < Y < Y_p. \tag{40}$$

with the following boundary conditions,

$$\Phi_2' = 0 \text{ at } Y = 0, \tag{41a}$$

$$\Phi_1 = \Phi_2, \qquad \Phi_1' = D_{21} \Phi_2' \text{ at } Y = Y_p, \tag{41b}$$

$$\Phi_1' = \lambda \Phi_1 \text{ at } Y = Y_0. \tag{41c}$$

By applying the boundary equations given in Eq. (41) to mass transfer Eqs. (39) and (40), the following expressions describing the species concentration profile across the microchannel are obtained,

$$\Phi_1(Y) = M_1 + M_2 Y - Sr_1 \theta_{nf1}(Y), \tag{42}$$

$$\Phi_2(Y) = M_3 - Sr_2 \theta_{nf2}(Y). \tag{43}$$

As previously stated, the analytical expressions for coefficients M_1 to M_3 were evaluated using a mathematical analysis tool due to their high complexity.

3. Results and discussion

3.1. Validation

To validate the model, the parameters were set such that the problem resembled those already investigated in the literature. In particular, the wall thickness was made negligible ($Y_0 \approx 1$), the catalytic layer and hence mass transfer were discarded, and the concentration of nanoparticles was reduced to zero. Hence, the temperature fields could be compared with the work of Karimi *et al.* [27] and the predictions for *Nu* could be compared to those presented in Ref. [50]. Figure 2 shows that graphs identical to those presented in the aforementioned works were successfully produced, thereby validating the analytical model developed in Section 2. Also, although not shown here, it was observed that in the limit of fully-filled microchannel and high *Bi* (thus LTE dominated), the observed trends in concentration profile were found to follow those documented in the work of Matin and Pop [19].

3.2. Temperature fields

In the subsequent case studies, the value of porosity has been set to 0.5. Figures 3a and 3b illustrate the influences of microchannel wall thickness upon the temperature profiles. Complexity of the temperature profiles is clearly depicted by these figures. In Fig. 3a, thickening the wall (that is decreasing the value of Y_0) has led to a significant increase in the dimensionless temperature of the external surface of the wall. The changes in the wall temperature through variation in the wall thickness can be explained by noting that the wall is transferring a constant heat flux and its thermal resistance is proportional to its thickness. Thus, thickening the wall increases the overall thermal resistance against transferring the heat flux to the microchannel and causes a general increase in the temperature of the system. Given the temperature sensitivity of most thermochemical reactions [1], such variation in the temperature fields is of practical significance and clearly demonstrates the necessity of including the microreactor walls in the thermal analysis of these systems. Further, the temperature changes imposed by the changes in the wall thickness have significantly affected the temperature profiles of the nanofluid and porous solid phases. A comparison between Figs. 3a and 3b reveals that the extent of these modifications is heavily dependent upon the interface model in use. Nonetheless, under both interface models, changes in the wall thickness can result in heat flux bifurcation [17][25][27]. This observation is of high importance in the design of microreactors as the direction of heat transfer in the porous region can influence the progress of homogenous chemical reactions.

Figures 3c and 3d show that by varying the thickness of the porous insert, a wealth of behaviours in the temperature fields can be observed. By comparing these two figures, it is seen that the thickness of the porous insert may play a more complex role on the temperature of different parts of the system under

Model A than Model B. In Model A, by increasing the value of porous thickness from 0.2 to 0.8, the temperature of the wall first decrease (for Y_p<0.8) and then increases. However, this behaviour for Model B is uniform and always decreasing. Reduction of the wall temperature for thicker porous inserts can be explained by noting that *Nu* generally increases by thickening the porous insert. Hence, the resultant enhancement of heat transfer rate leads to the reduction of the wall temperature. This behaviour has an important relation with the choice of the optimum thickness of the porous insert in the microchannel, which will be later discussed in further depth in relation to *Nu*.

Figure 4 shows the impact of the concentration of nanoparticles on the profiles of dimensionless temperatures across the microchannel. It is clearly seen that, for both cases, adding nanoparticles to the base fluid decreases the dimensionless temperature within the system and makes the temperature fields more uniform. This is to be expected, since by enhancing the concentration of nanoparticles the overall thermal conductivity of the fluid phase increases. Thus, the thermal energy can be more conveniently transferred to the microchannel with smaller temperature gradients, resulting in an overall reduction of the temperature. Interestingly, for both interface models, the concentration of the nanoparticles noticeably affects the dimensionless temperatures of the nanofluid phase and the wall. Yet, they hardly have any effect upon the temperature of the porous solid phase. This is, in part, due to the fact that the porous medium is located at the centre of the microreactor where, compared with the areas close to the walls, there is less heat to be extracted. Hence, adding nanoparticles to the base fluid does not have substantial impact on the temperature of the solid phase of the porous medium. Also, since Biot number has been kept constant in the analysis, the influences of increases in the concentration of nanoparticles upon the internal heat exchanges between the solid and nanofluid phases have been effectively ignored here. In keeping with that observed in Fig. 3, in Fig. 4 the predicted dimensionless temperatures under Model B are generally lower than those predicted by Model A. Once again, this has practical implications for the development tools to design and analyse of thermochemical microreactors.

3.3. Nusselt number

Figures 5-7 depict the variations of *Nu* versus thickness of the porous insert for different values of the pertinent parameters including the walls' thickness, nanoparticles concentration, volumetric internal heat generation of nanofluid within the microchannel, and the volumetric internal heat generation of solid phase of the porous section. As it can be seen from all of these figures, depending on the parametric values of the system, there is a certain value for Y_p which provides the maximum *Nu* within the microchannel. This is the

reason behind the changing behaviour of the temperature field while increasing Y_p from 0.6 to 0.8 in Figs. 3c and 3d. Also, by comparing parts *a* and *b* of each figure, two important conclusions can be drawn. The first one is that always Model B predicts a higher heat transfer rate than Model A (explaining why Model B temperature predictions in Fig. 3 are lower than those of Model A). This is a peculiarity of these two interface heat flux boundary conditions, and is consistent with *Nu* results reported in the partially-filled porous channel with zero wall thickness [24][20]. The second generic point is that for all cases, the optimum value of porous thickness for Model B is slightly larger than that under Model A.

Figure 5 shows that increasing the thickness of the walls increases the maximum value of *Nu* encountered in the microchannel quite significantly. This is such that by reducing Y_0 from 1 to 0.6, the maximum value of *Nu* is almost doubled. The physical reason for this behaviour can be explained by noting that the wall features internal heat generation and hence by thickening the wall the transported heat by the nanofluid flow within the microchannel has to be enhanced, which requires an increase in *Nu*. Figure 6 shows that increasing the nanoparticles concentration increases the *Nu* for both interface models and slightly shifts the optimum thickness of the porous insert towards larger values. Hence, by increasing the nanoparticles concentration, within the set of parametric values used in this figure, the thickness of the porous insert should slightly increase to achieve the maximum *Nu*. This is an important finding as establishes a link between the optimum thickness of the porous insert and the volumetric concentration of the nanoparticles.

Figure 7 depicts some interesting behaviours of *Nu* versus internal heat generations in the nanofluid and porous solid phases of the microchannel. Positive and negative values of ω_{nf} representing exothermic and endothermic chemical reactions in the nanofluid phase have been shown in Figs. 7a and 7b [51], while positive internal heat generations in the solid phase are shown in Figs. 7c and 7d. This figure shows that the maximum value of *Nu* is a very strong function of the internal heat generations in which exothermicity can substantially boost the *Nu*. Addition of heat to the system by the exothermicity of reactions increases the system temperature and consequently magnifies the temperature gradients, which are proportional to *Nu* [52]. In general, this sensitivity appears to be stronger under Model B. Yet, for both models the optimal thickness of the porous insert is only marginally affected by the variations in the heat generation. Further, under Model A there seems to be an inflection point for the dimensionless thickness of the porous insert at which the general behaviour of *Nu* changes. Figures 7a and 7c show that for $Y_p > 0.7$ increasing the

exothermicity of the nanofluid and porous solid phase reduces *Nu*. However, the existence of this inflection point is much less noticeable under Model B.

3.4. Concentration fields

Figures 8 to 12 have been devoted to the effects of different specifications of the microreactor on the concentration fields by implementing both porous-fluid interface models. It should be clarified that in this subsection, the concentration of the chemical species (consumed on the surface of the catalysts) is under investigation and the volumetric concentration of the nanoparticles is a parameter of the problem. One of the most apparent findings obtained through comparing Models A and B in Figs. 8 to 12 is that, with the used parametric values, Model B almost always predicts a lower concentration field than its companion. The reason for this can be attributed to the fact that in Model B the predicted temperature gradients are generally smaller than those predicted by Model A, and hence Soret effect is less influential on the concentration field. It is also clear that within the porous section of the microchannel the concentration profile is almost flat and significant homogenisation has been achieved compared with the open section of the microchannel.

Figure 8 shows that through decreasing the permeability of the porous medium the magnitude of the dimensionless concentration has decreases considerably. This is a clear manifestation of the thermal effects upon the diffusion of chemical species. It has been already demonstrated that in partially filled channels by reducing the permeability of the porous insert, the *Nu* increases [24], which reduces the temperature of the nanofluid phase and in turn weakens the thermal diffusion of mass. The net result is a smaller value of the dimensionless concentration through the Soret effect combined with the effects of first order chemical kinetics on the surface of the catalyst (see Eq. (11c)).

Figure 9 illustrates the effects of thicknesses of the walls and porous insert on the concentration field of the microchannel for both models. Figures 9a and 9b show that by increasing the walls' thickness, the value of dimensionless concentration increases over the entire cross section of the microchannel. Once again, this is closely related to the thermal behaviour of the system. Figure 3 showed that by thickening the microchannel walls, the dimensionless temperatures and the temperature gradients within the system increase significantly. These changes intensify the thermal diffusion of mass at higher wall thicknesses, and therefore cause and boost in the dimensionless concentration. It is interesting to note that increasing the walls' thickness from 0 to 0.2 increases the value of dimensionless concentration by almost 0.1 unit. However, further enlargement of the walls thickness (for the same amount) from 0.2 to 0.4 increases the

concentration field by around 0.4 unit. Figures 9c and 9d depict the effects of thickness of the porous insert upon the concertation field, while keeping the thickness of the walls constant. These figures indicate that increasing this thickness, magnifies the value of dimensionless concentration for both Models A and B. The most interesting observation here is the increment of concentration value for Model B by changing the porous thickness to 0.8. At this thickness of the porous insert the value of dimensionless concentration for Model B increases significantly and makes this case the only one with higher concentration compared to Model A for the same parametric values. This behaviour can be attributed to the temperature field for Model B at $Y_p = 0.8$, which has been illustrated in Fig. 3d.

Figure 10 depicts the effects of Soret numbers in the open and porous sections of the microchannel on the dimensionless concentration profiles for both Models A and B. The Sr_1 and Sr_2 are responsible for the thermal diffusion of mass in these regions and hence reflect the influences of the temperature field upon the concentration field in the open and porous sections of the microchannel, respectively. As expected, increasing the positive values of Soret number in the open and porous sections of the microchannel leads to larger values of dimensionless concentration. Physically, this implies that as the positive value of Soret number increases a lesser amount of chemical species is delivered to the catalyst and thus smaller amount of species are consumed. Consequently, at a given cross-section of the microchannel the concentration of species is higher for larger values of *Sr*. Comparison of the top sub-figures to the bottom ones in Fig. 10 reveals that the effect of *Sr* in the clear section on the concentration profiles is more pronounced. This can be readily explained by noting that the catalytic surface is in contact with the clear section of the microchannel.

Figure 11 is devoted to the effects of reaction rate on the concentration field and shows that reducing the negative value of Damköhler number the dimensionless concentration decreases under both models. This is due to the intensification of the catalytic reaction, which consumes more species and leads to the reduction of the concentration of species across the microchannel. Figure 11 also indicates that both models provide almost the same prediction for the influences of Damköhler number. Finally, Fig. 12 shows the effects of nanoparticles concentration on the concentration of chemical species, calculated for both interface models. The contents of this figure are totally consistent with those of Fig. 4 and show that the concentration of nanoparticles have a considerable influence upon the mass transfer. Augmenting the nanoparticle concentration leads to smaller values of dimensionless temperature and thus diminishes the Soret effect and results in smaller values of dimensionless concentration. Along with other figures

presented in this sub-section, Fig. 12 clearly demonstrates that modest manipulations of the thermal field in the microreactor can result in considerable changes in the mass transfer problem.

4. Conclusions

This paper puts forward a theoretical analysis of the double-diffusive forced convection in a microreactor partially filled with porous materials. The primary aim was to explore the influences of porous-fluid interface models, wall thickness and nanofluids upon the dispersion of mass, which was coupled with thermal fields through considering the Soret effect. A first order catalytic chemical reaction was considered on the walls and the wall thickness was included in the mathematical model. To augment heat transfer, nanoparticles were included in the base fluid. The momentum, energy and dispersion equations were analytically solved by taking an LTNE approach, and the temperature profiles, *Nu* and concentration profiles were illustrated. It was shown that the wall thickness has substantial impacts on all the aforementioned characteristics of the microreactor. It was also shown that the magnitude and the corresponding optimal thickness of the porous insert are strongly dependent upon the wall thickness. Most importantly, it was also observed that the thicknesses of the wall and porous insert have major influences on the uniformity and magnitude of the concentration profile, while the quantitative predictions are highly affected by the choice of the porous-fluid interface models. Further, the internal heat generations appeared to be of high significance in predicting the *Nu* of the system. As expected, the use of nanofluid led to an increase in the heat transfer within the microreactor, while it reduced the dimensionless concentration. Amongst other findings, this investigation revealed that by incorporating a centrally located porous insert and nanofluid in microreactors, the temperature and concentration profiles become more controllable.

Appendix A. Detailed solution procedure

A.1. Velocity distribution

Applying the dimensionless parameters defined in Eq. (25) to the momentum equations provides the following normalised relations for the velocity fields,

$$0 = 1 + C_\mu \frac{\partial^2 U_{nf}}{\partial Y^2} \quad \text{for} \quad Y_p < Y < Y_0, \tag{A1}$$

$$0 = 1 + \frac{\partial^2 U_p}{\partial Y^2} - \frac{C_\mu}{Y_0 Da} U_p \quad \text{for} \quad 0 < Y < Y_p, \tag{A2}$$

with the following associated boundary conditions,

$$\frac{\partial U_p}{\partial Y} = 0 \text{ at } Y = 0, \tag{A3a}$$

$$U_{nf} = U_p, \qquad C_\mu \frac{\partial U_{nf}}{\partial Y} = \frac{\partial U_p}{\partial Y} \text{ at } Y = Y_p, \tag{A3b}$$

$$U_{nf} = 0 \text{ at } Y = Y_0. \tag{A3c}$$

The resultant expressions for the dimensionless velocity in the clear and porous regions respectively are:

$$U_{nf}(Y) = -\frac{Y^2}{2C_\mu} + a + bY, \tag{A4}$$

$$U_p(Y) = \frac{Da\, Y_0}{C_\mu} + c\cosh(ZY), \tag{A5}$$

while the dimensionless average velocity for the flow is given by

$$\overline{U} = \frac{DaY_0Y_p}{C_\mu} + \frac{c}{Z}\sinh(ZY_p) - \frac{1}{6C_\mu}\left(Y_0^3 - Y_p^3\right) + \frac{1}{2}b\left(Y_0^2 - Y_p^2\right) + a\left(Y_0 - Y_p\right), \tag{A6}$$

where $Z = \sqrt{C_\mu/(Da\, Y_0)}$ and constants a, b and c are provided by:

$$a = -\frac{\left(-C_\mu Y_0^2 + 2C_\mu Y_0 Y_p\right)\cosh(ZY_p) + \left(ZY_0^2Y_p - 2DaZY_0^2 - ZY_0Y_p^2\right)\sinh(ZY_p)}{2C_\mu\left(C_\mu\cosh(ZY_p) + \left(ZY_0 - ZY_p\right)\sinh(ZY_p)\right)}, \tag{A7a}$$

$$b = -\frac{-2C_\mu Y_p\cosh(ZY_p) + \left(2DaZY_0 - ZY_0^2 + ZY_p^2\right)\sinh(ZY_p)}{2C_\mu(C_\mu\cosh(ZY_p) + (ZY_0 - ZY_p)\sinh(ZY_p)])}, \tag{A7b}$$

$$c = -\frac{(2DaY_0 - Y_0^2 + 2Y_0Y_p - Y_p^2)\ \mathrm{csch}\ (ZY_p)}{2\left(ZY_0 - ZY_p + C_\mu\coth(ZY_p)\right)}. \tag{A7c}$$

These velocity fields are hereafter used in the solution of the normalised equations for the heat flux at the porous-fluid interface, as well as the dimensionless energy equations.

By normalising Eq. (20) a dimensionless expression for Model A heat flux at the porous-fluid interface is produced. That is

$$\gamma_p\big|_{Model\ A} = \frac{\int_0^{Y_p} U_p dY}{\overline{U}}\left(1 + Q_1(1 - Y_0) + \omega_s Y_p + \omega_{nf}Y_0\right) - \left(\omega_s + \omega_{nf}\right)Y_p, \tag{A8}$$

and the substitution of Eqs. (A5) and (A6) reveals

$$\gamma_p\big|_{Model\ A} = \frac{\frac{Da}{C_\mu}Y_0Y_p + \frac{c}{Z}\sinh(ZY_p)}{a\left(Y_0 - Y_p\right) + \frac{Da}{C_\mu}Y_0Y_p + \frac{1}{2}\,\mathrm{b}\left(Y_0^2 - Y_p^2\right) - \frac{1}{6\,C_\mu}\left(Y_0^3 - Y_p^3\right) + \frac{c}{Z}\sinh(ZY_p)} \tag{A9}$$

$$\times\left(1 + Q_1(1 - Y_0) + \omega_s Y_p + \omega_{nf}Y_0\right) - \left(\omega_s + \omega_{nf}\right)Y_p.$$

Similarly, normalising Eq. (23) provides an expression for the dimensionless form of Model B heat flux at the porous-fluid interface:

$$\gamma_p\big|_{Model\ B} = \frac{\int_0^{Y_p} U_p dY}{2\overline{U}-\int_0^{Y_p} U_p dY} - \frac{\overline{U}}{2\overline{U}-\int_0^{Y_p} U_p dY} \times \left[\left(\omega_s + \omega_{nf}\right) Y_p - \frac{\int_0^{Y_p} U_p dY}{\overline{U}} \left(Q_1(1-Y_0) + \omega_{nf} Y_0 + \omega_s Y_p \right) \right], \tag{A10}$$

and through substitution of Eqs. (A5) and (A6) this expands to:

$$\begin{aligned} &\gamma_p\big|_{Model\ B} \\ &= \frac{\frac{DaY_0}{C_\mu} Y_p + \frac{c}{Z}\sinh(ZY_p)}{2\left(a(Y_0 - Y_p) + \frac{Da}{C_\mu} Y_0 Y_p + \frac{1}{2} b(Y_0^2 - Y_p^2) - \frac{1}{6C_\mu}(Y_0^3 - Y_p^3) + \frac{c}{Z}\sinh(ZY_p)\right) - \frac{Da}{C_\mu} Y_0 Y_p - \frac{c}{Z}\sinh(ZY_p)} \\ &- \frac{a\left(Y_0 - Y_p\right) + \frac{Da}{C_\mu} Y_0 Y_p + \frac{1}{2} b\left(Y_0^2 - Y_p^2\right) - \frac{1}{6C_\mu}\left(Y_0^3 - Y_p^3\right) + \frac{c}{Z}\sinh\left(ZY_p\right)}{2\left(a\left(Y_0 - Y_p\right) + \frac{Da}{C_\mu} Y_0 Y_p + \frac{1}{2} b\left(Y_0^2 - Y_p^2\right) - \frac{1}{6C_\mu}\left(Y_0^3 - Y_p^3\right) + \frac{c}{Z}\sinh\left(ZY_p\right)\right) - \frac{Da}{C_\mu} Y_0 Y_p - \frac{c}{Z}\sinh\left(ZY_p\right)} \\ &\times \left[\left(\omega_{nf} + \omega_s\right) Y_p - \frac{\left(Q_1(1-Y_0) + \omega_{nf} Y_0 + \omega_s Y_p\right)\left(\frac{DaY_0}{C_\mu} Y_p + \frac{c}{Z}\sinh\left(ZY_p\right)\right)}{a\left(Y_0 - Y_p\right) + \frac{Da}{C_\mu} Y_0 Y_p + \frac{1}{2} b\left(Y_0^2 - Y_p^2\right) - \frac{1}{6C_\mu}\left(Y_0^3 - Y_p^3\right) + \frac{c}{Z}\sinh\left(ZY_p\right)} \right]. \end{aligned} \tag{A11}$$

Finally, the dimensionless form of the fluid-wall heat flux is given by

$$\gamma_s = 1 + (Q_1 - Y_0). \tag{A12}$$

A.2. Model A prediction of the temperature fields

Through substitution of the normalised quantities presented in Eq. (25), dimensionless versions of Eqs. (3)-(6) can be produced for the Model A predictions of the temperature fields. Thus, the transport of thermal energy for the solid wall, open region, and nanofluid and solid phases of the porous region, respectively become,

$$\theta_1''(Y) + \frac{Q_1}{k_{1s}} = 0, \tag{A13}$$

$$\frac{U_{nf}(Y)}{\overline{U}}\left(1 + Q_1(1-Y_0) + \omega_{nf} Y_0 + \omega_s Y_p\right) = \frac{C_k Y_0}{k\varepsilon}\theta_{nf1}''(Y) + \omega_{nf} Y_0, \tag{A14}$$

$$\begin{aligned} &\frac{U_p(Y)}{\overline{U}}\left(1 + Q_1(1-Y_0) + \omega_{nf} Y_0 + \omega_s Y_p\right) \\ &= \frac{C_k Y_0}{k}\theta_{nf2}''(Y) + \frac{Bi}{Y_0}\left(\theta_s(Y) - \theta_{nf2}(Y)\right) + \omega_{nf} Y_0, \end{aligned} \tag{A15}$$

$$0 = \theta_s''(Y) - \frac{Bi}{Y_0}\Big(\theta_s(Y) - \theta_{nf2}(Y)\Big) + \omega_s. \tag{A16}$$

Furthermore, the associated dimensionless boundary conditions under Model A assumption are as follows,

$$\theta_{nf2}'(0) = \theta_s'(0) = 0, \tag{A17a}$$

$$\theta_{nf1}(Y_p) = \theta_{nf2}(Y_p) = \theta_s(Y_p) = 0, \tag{A17b}$$

$$\theta_{nf1}(Y_0) = \theta_1(Y_0)\frac{C_k}{k\varepsilon}, \tag{A17c}$$

$$\theta_{nf1}'(Y_0) = \theta_1'(Y_0), \tag{A17d}$$

$$k_{1s}\theta_1'(1) = \frac{1}{k_{1s}}. \tag{A17e}$$

By taking the second derivative with respect to Y, coupled Eqs. (A15) and (A16) can be decoupled and turned into fourth order ODE's of the following forms,

$$\begin{aligned}\theta_{nf2}''''(Y) - \frac{Bi}{Y_0}\left(1 + \frac{k}{C_k Y_0}\right)\theta_{nf2}''(Y) \\ = \frac{k}{C_k Y_0}\big(1 + Q_1(1 - Y_0) + \omega_{nf}Y_0 + \omega_s Y_p\big) \times \left[\frac{U_p''(Y)}{\overline{U}} - \frac{Bi}{Y_0}\frac{U_p(Y)}{\overline{U}}\right] \\ + \frac{kBi}{C_k Y_0^2}(\omega_n f Y_0 + \omega_s),\end{aligned} \tag{A18}$$

$$\begin{aligned}\theta_s''''(Y) - \frac{Bi}{Y_0}\left(1 + \frac{k}{C_k Y_0}\right)\theta_s''(Y) \\ = \frac{Bik}{C_k Y_0^2}\left[\frac{U_p(Y)}{\overline{U}}\big(1 + Q_1(1 - Y_0) + \omega_{nf}Y_0 + \omega_s Y_p\big) - \big(\omega_{nf}Y_0 + \omega_s\big)\right].\end{aligned} \tag{A19}$$

Evaluating the second and third derivatives of θ_s and θ_{nf2} at $Y = Y_p$ and $Y = 0$, respectively, the following boundary conditions are revealed,

$$\theta_{nf2}'''(0) = \theta_s'''(0) = 0, \tag{A20a}$$

$$\theta_{nf2}''(Y_p) = \frac{k}{C_k Y_0}\left[\frac{U_p(Y_p)}{\overline{U}}\big(1 + Q_1(1 - Y_0) + \omega_{nf}Y_0 + \omega_s Y_p\big) - \omega_{nf}Y_0\right], \tag{A20b}$$

$$\theta_s''(Y_p) = -\omega_s. \tag{A20c}$$

By solving decoupled energy Eqs. (A13), (A14), (A18) and (A19) and applying the boundary conditions given by Eqs. (A17) and (A20), expressions for the Model A temperature fields across the microchannel can be obtained. Firstly, for the solid wall:

$$\theta_1(Y) = -\frac{Q_1 Y^2}{2k_{1s}} + A_1 + A_2 Y, \tag{A21}$$

and the temperature field for the clear region is given by

$$\theta_{nf1}(Y) = Y^3 b \frac{k\varepsilon\chi_A}{6C_k\overline{U}Y_0} - Y^4 \frac{k\varepsilon\chi_A}{24C_kC_\mu\overline{U}Y_0} + Y^2\left(-\frac{k\omega_{nf}\varepsilon}{2C_k} + a\frac{k\varepsilon\chi_A}{2C_k\overline{U}Y_0}\right) + A_3 + A_4 Y. \tag{A22}$$

Further, the temperature fields for the nanofluid and solid phases of the porous region are respectively resolved to the following forms,

$$\begin{aligned}\theta_{nf2}(Y) = &-\frac{kY^2\left(C_\mu\overline{U}\omega_s + C_\mu\overline{U}\omega_{nf}Y_0 - DaY_0\chi_A\right)}{2C_\mu\overline{U}(k + C_kY_0)} + A_5\frac{C_kY_0^2}{Bi(k + C_kY_0)}\cosh(\alpha Y) + A_6 \\ &+ c\frac{k(-Bi + Y_0Z^2)\chi_A}{\overline{U}Z^2(-kBi - BiC_kY_0 + C_kY_0^2Z^2)}\cosh(ZY),\end{aligned} \tag{A23}$$

$$\begin{aligned}\theta_s(Y) = &-\frac{kY^2\left(C_\mu\overline{U}\omega_s + C_\mu\overline{U}\omega_{nf}Y_0 - DaY_0\chi_A\right)}{2C_\mu\overline{U}(k + C_kY_0)} + A_7\frac{C_kY_0^2}{Bi(k + C_kY_0)}\cosh(\alpha Y) + A_8 \\ &+ c\frac{kBi\chi_A}{\overline{U}Z^2(kBi + BiC_kY_0 - C_kY_0^2Z^2)}\cosh(ZY),\end{aligned} \tag{A24}$$

where $\chi_A = (1 + Q_1(1 - Y_0) + \omega_{nf}Y_0 + \omega_sY_p)$, $\alpha = \frac{\sqrt{Bi}\sqrt{k+C_kY_0}}{\sqrt{C_k}Y_0}$ and constants a, b and c are provided by Eq. (A7). Coefficients A_1 to A_8 are lengthy algebraic expressions, which do not specifically reveal any information of interest and hence, in the interest of conciseness, are not provided here.

A.3. Model B predictions of the temperature fields

Under the conditions for Model B, the transport of energy for the solid wall and the solid phase of the porous region are unchanged from their form under Model A, and thus are already provided by Eqs. (A13) and (A14). Normalised versions of Eqs. (4) and (5) under Model B are generated by applying the relevant dimensionless variables introduced in Eq. (25). The transport of energy for the nanofluid in the clear region under Model B reduces to

$$\frac{U_{nf}(Y)}{\overline{U}}\left(1 + \gamma_p|_{Model\ B} + Q_1(1 - Y_0) + \omega_{nf}Y_0 + \omega_sY_p\right) = \frac{C_kY_0}{k\varepsilon}\theta''_{nf1}(Y) + \omega_{nf}Y_0, \tag{A25}$$

and for the nanofluid phase inside the porous region, it becomes:

$$\begin{aligned}&\frac{U_p(Y)}{\overline{U}}\left(1 + \gamma_p|_{ModelB} + Q_1(1 - Y_0) + \omega_{nf}Y_0 + \omega_sY_p\right) \\ &\qquad = \frac{C_kY_0}{k}\theta''_{nf2}(Y) + \frac{Bi}{Y_0}\left(\theta_s(Y) - \theta_{nf2}(Y)\right) + \omega_{nf}Y_0.\end{aligned} \tag{A26}$$

The corresponding boundary conditions for Model B are as follows

$$\theta'_{nf2}(0) = \theta'_s(0) = 0, \tag{A27a}$$

$$\theta_{nf1}(Y_p) = \theta_{nf2}(Y_p), \tag{A27b}$$

$$\theta_s(Y_p) = 0, \tag{A27c}$$

$$\frac{C_k}{k}\theta'_{nf2}(Y_p) = \theta'_s(Y_p) = \gamma_p|_{Model\ B}, \tag{A27d}$$

$$\theta''_s(Y_p) + \frac{Bi}{Y_0}\theta_{nf2}(Y_p) + \omega_s = 0, \tag{A27e}$$

$$\theta_{nf1}(Y_0) = \theta_1(Y_0), \tag{A27f}$$

$$\frac{C_k}{k\varepsilon}\,\theta'_{nf1}(Y_0) = \theta'_1(Y_0)\,k_{1s}, \tag{A27g}$$

$$\theta'_1(1) = \frac{1}{k_{1s}}. \tag{A27h}$$

In order to decouple energy equations of the porous region, given by Eqs. (A15) and (A16), the second derivative is taken with respect to Y. Some algebraic manipulations result in

$$\begin{aligned}\theta''''_{nf2}(Y) - \frac{Bi}{Y_0}\left(1 + \frac{k}{C_k Y_0}\right)\theta''_{nf2}(Y) \\ = \frac{k}{C_k Y_0}\left(1 + \gamma_p|_{Model\ B} + Q_1(1 - Y_0) + \omega_{nf}Y_0 + \omega_s Y_p\right) \\ \times\left[\frac{U''_p(Y)}{\overline{U}} - \frac{Bi}{Y_0}\frac{U_p(Y)}{\overline{U}}\right] + \frac{kBi}{C_k Y_0^2}(\omega_n f Y_0 + \omega_s),\end{aligned} \tag{A28}$$

$$\begin{aligned}\theta''''_s(Y) - \frac{Bi}{Y_0}\left(1 + \frac{k}{C_k Y_0}\right)\theta''_s(Y) \\ = \frac{Bi\,k}{C_k Y_0^2}\left[\frac{U_p(Y)}{\overline{U}}\left(1 + \gamma_p|_{Model\ B} + Q_1(1 - Y_0) + \omega_{nf}Y_0 + \omega_s Y_p\right)\right. \\ \left. - \left(\omega_{nf}Y_0 + \omega_s\right)\right].\end{aligned} \tag{A29}$$

Evaluating the second and third derivatives of θ_s and θ_{nf2} at $Y = 0$ reveals

$$\theta'''_{nf2}(0) = \theta'''_s(0) = 0. \tag{A30}$$

By solving the ODE's presented in Eqs. (A13), (A25), (A28) and (A29), which represent the transport of energy across each section of the microchannel, a full representation of the temperature field at each point across the system is established. For the solid wall:

$$\theta_1(Y) = -\frac{Q_1 Y^2}{2k_{1s}} + B_1 + B_2 Y, \tag{A31}$$

and for the nanofluid in the clear region:

$$\theta_{nf1}(Y) = Y^3 b \frac{k\varepsilon\chi_B}{6C_k\overline{U}Y_0} - Y^4 \frac{k\varepsilon\chi_B}{24C_kC_\mu\overline{U}Y_0} + Y^2\left(-\frac{k\omega_{nf}\varepsilon}{2C_k} + a\frac{k\varepsilon\chi_B}{2C_k\overline{U}Y_0}\right) + B_3 + B_4 Y. \tag{A32}$$

The temperature fields of the nanofluid and solid phases of the porous region are given by

$$\theta_{nf2}(Y) = -\frac{kY^2\left(C_\mu\overline{U}\omega_s + C_\mu\overline{U}\omega_{nf}Y_0 - DaY_0\chi_B\right)}{2C_\mu\overline{U}(k + C_kY_0)} + B_5\frac{C_kY_0^2}{Bi(k + C_kY_0)}\cosh(\alpha Y) + B_6 + c\frac{k(-Bi + Y_0Z^2)\chi_B}{\overline{U}Z^2(-kBi - BiC_kY_0 + C_kY_0^2Z^2)}\cosh(ZY), \tag{A33}$$

$$\theta_s(Y) = -\frac{kY^2\left(C_\mu\overline{U}\omega_s + C_\mu\overline{U}\omega_{nf}Y_0 - DaY_0\chi_B\right)}{2C_\mu\overline{U}(k + C_kY_0)} + B_7\frac{C_kY_0^2}{Bi(k + C_kY_0)}\cosh(\alpha Y) + B_8 + c\frac{kBi\chi_B}{\overline{U}Z^2(kBi + BiC_kY_0 - C_kY_0^2Z^2)}\cosh(ZY), \tag{A34}$$

where $\chi_B = (1 + \gamma_p|_{Model\ B} + Q_1(1 - Y_0) + \omega_{nf}Y_0 + \omega_sY_p)$, $\alpha = \frac{\sqrt{Bi}\sqrt{k+C_kY_0}}{\sqrt{C_k}Y_0}$ and constants a, b and c are provided by Eq. (A7). Once again, coefficients B_1 to B_8 are very long algebraic expressions and thus are not given in here.

A.4. LTE solution

The local thermal equilibrium state in the porous region can be derived by adding Eqs. (A15) and (A16) to produce,

$$\frac{U_p(Y)}{\overline{U}}\left(1 + Q_1(1 - Y_0) + \omega_{nf}Y_0 + \omega_sY_p\right) = \frac{C_kY_0}{k}\theta''_{nf2}(Y) + \theta''_s(Y) + \omega_{nf}Y_0 + \omega_s, \tag{A35}$$

and by applying the LTE condition of $\theta_{nf2} = \theta_s = \theta_{LTE}$ the following one-equation model is developed:

$$\frac{U_p(Y)}{\overline{U}}\left(1 + Q_1(1 - Y_0) + \omega_{nf}Y_0 + \omega_sY_p\right) = \left(\frac{C_kY_0}{k} + 1\right)\theta''_{LTE}(Y). \tag{A36}$$

The related boundary conditions for the LTE model reduce to

$$\theta'_{LTE}(0) = 0, \tag{A37a}$$

$$\theta_{LTE}(Y_p) = \theta_{nf1}(Y_p). \tag{A37b}$$

By integrating Eq. (A36) and applying the boundary conditions provided in Eq. (A37), the LTE temperature field can be defined as

$$\theta_{LTE}(Y) = C_{LTE} + \frac{k\left(-\frac{1}{2}C_\mu\overline{U}Y^2(\omega_{nf}Y_0 + \omega_s) + \chi\left[\frac{1}{2}DaY_0Y^2 + \frac{c}{Z^2}C_\mu\cosh(ZY)\right]\right)}{C_\mu\overline{U}(k + C_\mu Y_0)}, \tag{A38}$$

where $\chi = (1 + Q_1(1 - Y_0) + \omega_{nf}Y_0 + \omega_sY_p)$ and coefficient C_{LTE} consists of lengthy long-form algebra not provided here.

References

[1] Kolb G. Review: Microstructured reactors for distributed and renewable production of fuels and electrical energy. Chem Eng Process Process Intensif 2013;65:1–44. doi:10.1016/j.cep.2012.10.015.

[2] Yao X, Zhang Y, Du L, Liu J, Yao J. Review of the applications of microreactors. Renew Sustain Energy Rev 2015;47:519–39. doi:10.1016/j.rser.2015.03.078.

[3] Wirth T. Microreactors in Organic Synthesis and Catalysis. John Wiley & Sons; 2013. doi:10.1002/9783527622856.

[4] Tanimu A, Jaenicke S, Alhooshani K. Heterogeneous catalysis in continuous flow microreactors: A review of methods and applications. Chem Eng J 2017;327:792–821. doi:10.1016/j.cej.2017.06.161.

[5] Roberge DM, Ducry L, Bieler N, Cretton P, Zimmermann B. Microreactor technology: A revolution for the fine chemical and pharmaceutical industries? Chem Eng Technol 2005;28:318–23. doi:10.1002/ceat.200407128.

[6] Mies MJM, Rebrov E V., Deutz L, Kleijiv CR, De Croon MHJM, Schouten JC. Experimental validation of the performance of a microreactor for the high-throughput screening of catalytic coatings. Ind Eng Chem Res 2007;46:3922–31. doi:10.1021/ie061081w.

[7] Pallares J, Ferré JA. A simple model to predict mass transfer rates and kinetics of biochemical and biomedical Michaelis-Menten surface reactions. Int J Heat Mass Transf 2015;80:192–8. doi:10.1016/j.ijheatmasstransfer.2014.09.008.

[8] Tang Y, Rao L, Li Z, Lu H, Yan C, Yu S, et al. Rapid synthesis of highly photoluminescent nitrogen-doped carbon quantum dots via a microreactor with foamy copper for the detection of Hg2+ions. Sensors Actuators, B Chem 2018;258:637–47. doi:10.1016/j.snb.2017.11.140.

[9] Götz M, Lefebvre J, Mörs F, McDaniel Koch A, Graf F, Bajohr S, et al. Renewable Power-to-Gas: A technological and economic review. Renew Energy 2016;85:1371–90. doi:10.1016/j.renene.2015.07.066.

[10] Hunt G, Karimi N, Torabi M. Two-dimensional analytical investigation of coupled heat and mass transfer and entropy generation in a porous, catalytic microreactor. Int J Heat Mass Transf 2018;119:372–91. doi:10.1016/j.ijheatmasstransfer.2017.11.118.

[11] Chen Y, Shen C, Shi M, Peterson GP. Visualization study of flow condensation in hydrophobic microchannels. AIChE J 2014;60:1182–1192. doi:10.1002/aic.

[12] Elias Y, Rudolf von Rohr P, Bonrath W, Medlock J, Buss A. A porous structured reactor for hydrogenation reactions. Chem Eng Process Process Intensif 2015;95:175–85. doi:10.1016/j.cep.2015.05.012.

[13] Munirathinam R, Huskens J, Verboom W. Supported catalysis in continuous-flow microreactors. Adv Synth Catal 2015;357:1093–123. doi:10.1002/adsc.201401081.

[14] Buonomo B, Manca O, Lauriat G. Forced convection in micro-channels filled with porous media in local thermal non-equilibrium conditions. Int J Therm Sci 2014;77:206–22. doi:10.1016/j.ijthermalsci.2013.11.003.

[15] Wang K, Tavakkoli F, Vafai K. Analysis of gaseous slip flow in a porous micro-annulus under local thermal non-equilibrium condition - An exact solution. Int J Heat Mass Transf 2015;89:1331–41. doi:10.1016/j.ijheatmasstransfer.2015.06.001.

[16] Torabi M, Karimi N, Peterson GP, Yee S. Challenges and progress on the modeling of entropy generation in porous media: A review. Int J Heat Mass Transf 2017;114:31–46. doi:http://dx.doi.org/10.1016.

[17] Torabi M, Karimi N, Zhang K, Peterson GP. Generation of entropy and forced convection of heat in a conduit partially filled with porous media – Local thermal non-equilibrium and exothermicity effects. Appl Therm Eng 2016;106:518–36. doi:10.1016/j.applthermaleng.2016.06.036.

[18] Torabi M, Torabi M, Peterson GP. Entropy generation of double diffusive forced convection in porous channels with thick walls and Soret effect. Entropy 2017;19:171. doi:10.3390/e19040171.

[19] Matin MH, Pop I. Forced convection heat and mass transfer flow of a nanofluid through a porous channel with a first order chemical reaction on the wall. Int Commun Heat Mass Transf 2013;46:134–41. doi:10.1016/j.icheatmasstransfer.2013.05.001.

[20] Torabi M, Dickson C, Karimi N. Theoretical investigation of entropy generation and heat transfer by forced convection of copper–water nanofluid in a porous channel — Local thermal non-equilibrium and partial filling effects. Powder Technol 2016;301:234–54. doi:10.1016/j.powtec.2016.06.017.

[21] Yang K, Vafai K. Restrictions on the validity of the thermal conditions at the porous-fluid interface—An exact solution. J Heat Transfer 2011;133:112601. doi:10.1115/1.4004350.

[22] Hunt G, Torabi M, Govone L, Karimi N, Mehdizadeh A. Two-dimensional heat and mass transfer and thermodynamic analyses of porous microreactors with Soret and thermal radiation effects—An analytical approach. Chem Eng Process - Process Intensif 2018;126. doi:10.1016/j.cep.2018.02.025.

[23] Govone L, Torabi M, Wang L, Karimi N. Effects of nanofluid and radiative heat transfer on the double-diffusive forced convection in microreactors. J Therm Anal Calorim 2018. doi:10.1007/s10973-018-7027-z.

[24] Dickson C, Torabi M, Karimi N. First and second law analyses of nanofluid forced convection in a partially-filled porous channel – The effects of local thermal non-equilibrium and internal heat sources. Appl Therm Eng 2016;103:459–80. doi:10.1016/j.applthermaleng.2016.04.095.

[25] Torabi M, Karimi N, Zhang K. Heat transfer and second law analyses of forced convection in a channel partially filled by porous media and featuring internal heat sources. Energy 2015;93:106–27. doi:10.1016/j.energy.2015.09.010.

[26] Karimi N, Mahmoudi Y, Mazaheri K. Temperature fields in a channel partially filled with a porous material under local thermal non-equilibrium condition - An exact solution. Proc Inst Mech Eng Part C J Mech Eng Sci 2014;288:2778–89. doi:10.1177/0954406214521800.

[27] Karimi N, Agbo D, Talat Khan A, Younger PL. On the effects of exothermicity and endothermicity upon the temperature fields in a partially-filled porous channel. Int J Therm Sci 2015;96:128–48. doi:10.1016/j.ijthermalsci.2015.05.002.

[28] Hunt G, Karimi N, Torabi M. Analytical investigation of heat transfer and classical entropy generation in microreactors - The influences of exothermicity and asymmetry. Appl Therm Eng 2017;119:403–24. doi:10.1016/j.applthermaleng.2017.03.057.

[29] Elliott A, Torabi M, Karimi N. Thermodynamics analyses of porous microchannels with asymmetric thick walls and exothermicity: An entropic model of microreactors. J Therm Sci Eng Appl 2017;9:041013. doi:10.1115/1.4036802.

[30] Elliott A, Torabi M, Karimi N, Cunningham S. On the effects of internal heat sources upon forced convection in porous channels with asymmetric thick walls. Int Commun Heat Mass Transf 2016;73:100–10. doi:10.1016/j.icheatmasstransfer.2016.02.016.

[31] Kolb G, Hessel V. Micro-structured reactors for gas phase reactions. Chem Eng J 2004;98:1–38. doi:10.1016/j.cej.2003.10.005.

[32] Guthrie DGP, Torabi M, Karimi N. Energetic and entropic analyses of double-diffusive, forced convection heat and mass transfer in microreactors assisted with nanofluid. J Therm Anal Calorim 2018;3. doi:10.1007/s10973-018-7959-3.

[33] Claiborne HC, Solomito M, Ritts JJ. Heat generation by neutrons in some moderating and shielding

materials. Nucl Eng Des 1971;15:232–6.

[34] Bandhauer TM, Garimella S, Fuller TF. A critical review of thermal issues in lithium-ion batteries. J Electrochem Soc 2011;158:R1–25. doi:10.1149/1.3515880.

[35] Haber J, Kashid MN, Borhani N, Thome J, Krtschil U, Renken A, et al. Infrared imaging of temperature profiles in microreactors for fast and exothermic reactions. Chem Eng J 2013;214:97–105. doi:10.1016/j.cej.2012.10.021.

[36] Nield DA, Bejan A. Convection in Porous Media. 4th editon. New York: Speringer; 2013.

[37] Pallares J. Local mass transfer rates of a first-order chemical reaction on a wall: Application to the prediction of local platelet deposition in a perfusion chamber. Int J Heat Mass Transf 2015;90:254–8. doi:10.1016/j.ijheatmasstransfer.2015.06.062.

[38] Jejurkar SY, Mishra DP. Numerical analysis of entropy generation in an annular microcombustor using multistep kinetics. Appl Therm Eng 2013;52:394–401. doi:10.1016/j.applthermaleng.2012.12.021.

[39] Deen WM. Analysis of transport phenomena. Oxford University Press; 1998.

[40] Vafai K. Handbook of Porous Media. Third Edi. CRC Press; 2015.

[41] Chen WH, Cheng TC, Hung CI. Modeling and simulation of microwave double absorption on methanol steam reforming for hydrogen production. Int J Hydrogen Energy 2011;36:333–44. doi:10.1016/j.ijhydene.2010.09.009.

[42] Chen WH, Cheng TC, Hung CI. Numerical predictions on thermal characteristic and performance of methanol steam reforming with microwave-assisted heating. Int J Hydrogen Energy 2011;36:8279–91. doi:10.1016/j.ijhydene.2011.04.145.

[43] Silva RA, de Lemos MJS. Turbulent flow in a channel occupied by a porous layer considering the stress jump at the interface. Int J Heat Mass Transf 2003;46:5113–21. doi:10.1016/S0017-9310(03)00368-5.

[44] Masciarelli CB, de Lemos MJS. A new numerical scheme for using the two-energy equation model for turbulent buoyant flow in a composite enclosure. Numer Heat Transf Part B Fundam 2018;74:578–602. doi:10.1080/10407790.2018.1541291.

[45] Alazmi B, Vafai K. Constant wall heat flux boundary conditions in porous media under local thermal non-equilibrium conditions. Int J Heat Mass Transf 2002;45:3071–87.

[46] Yang K, Vafai K. Analysis of heat flux bifurcation inside porous media incorporating inertial and

dispersion effects – An exact solution. Int J Heat Mass Transf 2011;54:5286–97. doi:10.1016/j.ijheatmasstransfer.2011.08.014.

[47] Khanafer K, Vafai K. A critical synthesis of thermophysical characteristics of nanofluids. Int J Heat Mass Transf 2011;54:4410–28. doi:10.1016/j.ijheatmasstransfer.2011.04.048.

[48] Sundar LS, Sharma K V., Naik MT, Singh MK. Empirical and theoretical correlations on viscosity of nanofluids: A review. Renew Sustain Energy Rev 2013;25:670–86. doi:10.1016/j.rser.2013.04.003.

[49] Rohsenow W, Hartnett J, Cho Y. Hand book of heat transfer. 1998. doi:10.1016/0017-9310(75)90148-9.

[50] Mahmoudi Y, Karimi N, Mazaheri K. Analytical investigation of heat transfer enhancement in a channel partially filled with a porous material under local thermal non-equilibrium condition: Effects of different thermal boundary conditions at the porous-fluid interface. Int J Heat Mass Transf 2014;70:875–91. doi:10.1016/j.ijheatmasstransfer.2013.11.048.

[51] Rahimpour MR, Dehnavi MR, Allahgholipour F, Iranshahi D, Jokar SM. Assessment and comparison of different catalytic coupling exothermic and endothermic reactions: A review. Appl Energy 2012;99:496–512. doi:10.1016/j.apenergy.2012.04.003.

[52] Bergman TL, Lavine AS, Incropera FP, DeWitt DP. Introduction to Heat Transfer. 6th ed. John Wiley and Sons, Inc.; 2011.

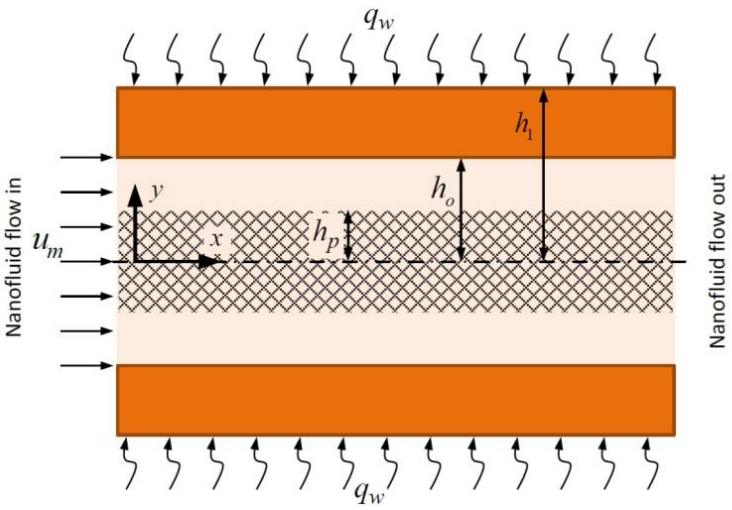

Fig. 1. Schematic configurations of the model microreactor.

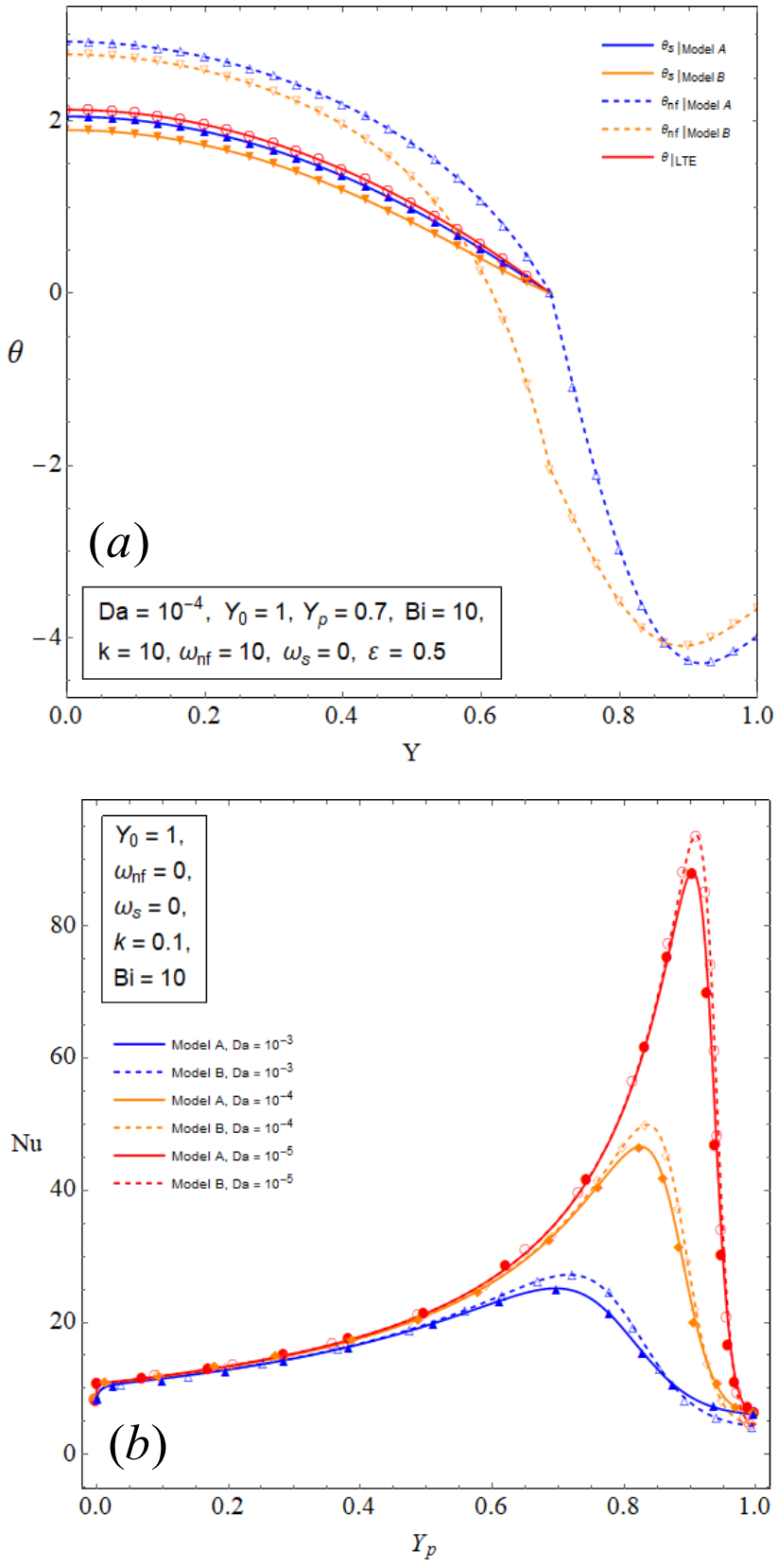

Fig. 2. Comparison of the present solution (symbols) with (*a*) temperature fields of Ref. [27] (lines) and (*b*) *Nu* of Ref. [50] (lines) for both models.

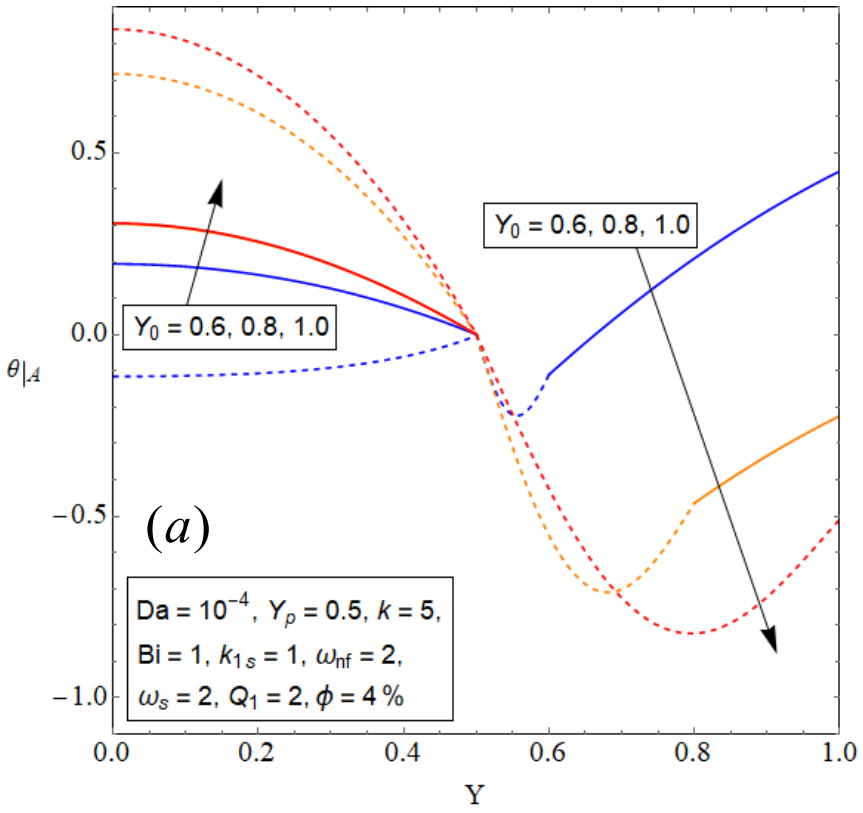
0.5
0.0
−0.5
−1.0
$\theta|_A$
Y_0 = 0.6, 0.8, 1.0
Y_0 = 0.6, 0.8, 1.0
(a)
Da = 10^{-4}, Y_p = 0.5, k = 5,
Bi = 1, k_{1s} = 1, ω_{nf} = 2,
ω_s = 2, Q_1 = 2, ϕ = 4 %
0.0
0.2
0.4
0.6
0.8
1.0
Y

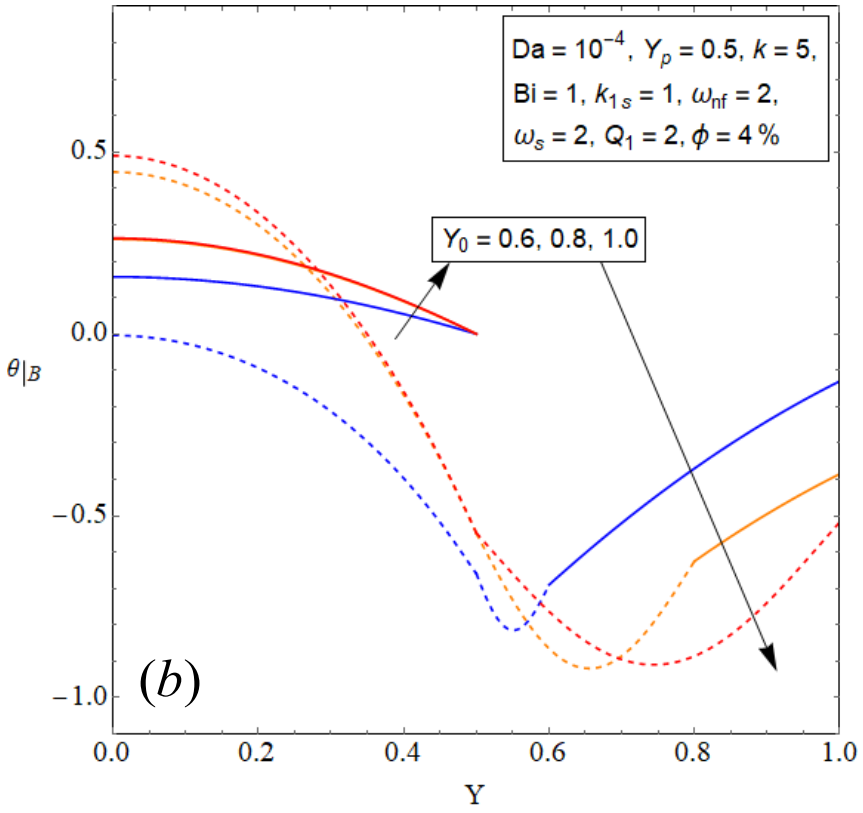
Da = 10^{-4}, Y_p = 0.5, k = 5,
Bi = 1, k_{1s} = 1, ω_{nf} = 2,
ω_s = 2, Q_1 = 2, ϕ = 4 %
Y_0 = 0.6, 0.8, 1.0
0.5
0.0
−0.5
−1.0
$\theta|_B$
(b)
0.0
0.2
0.4
0.6
0.8
1.0
Y

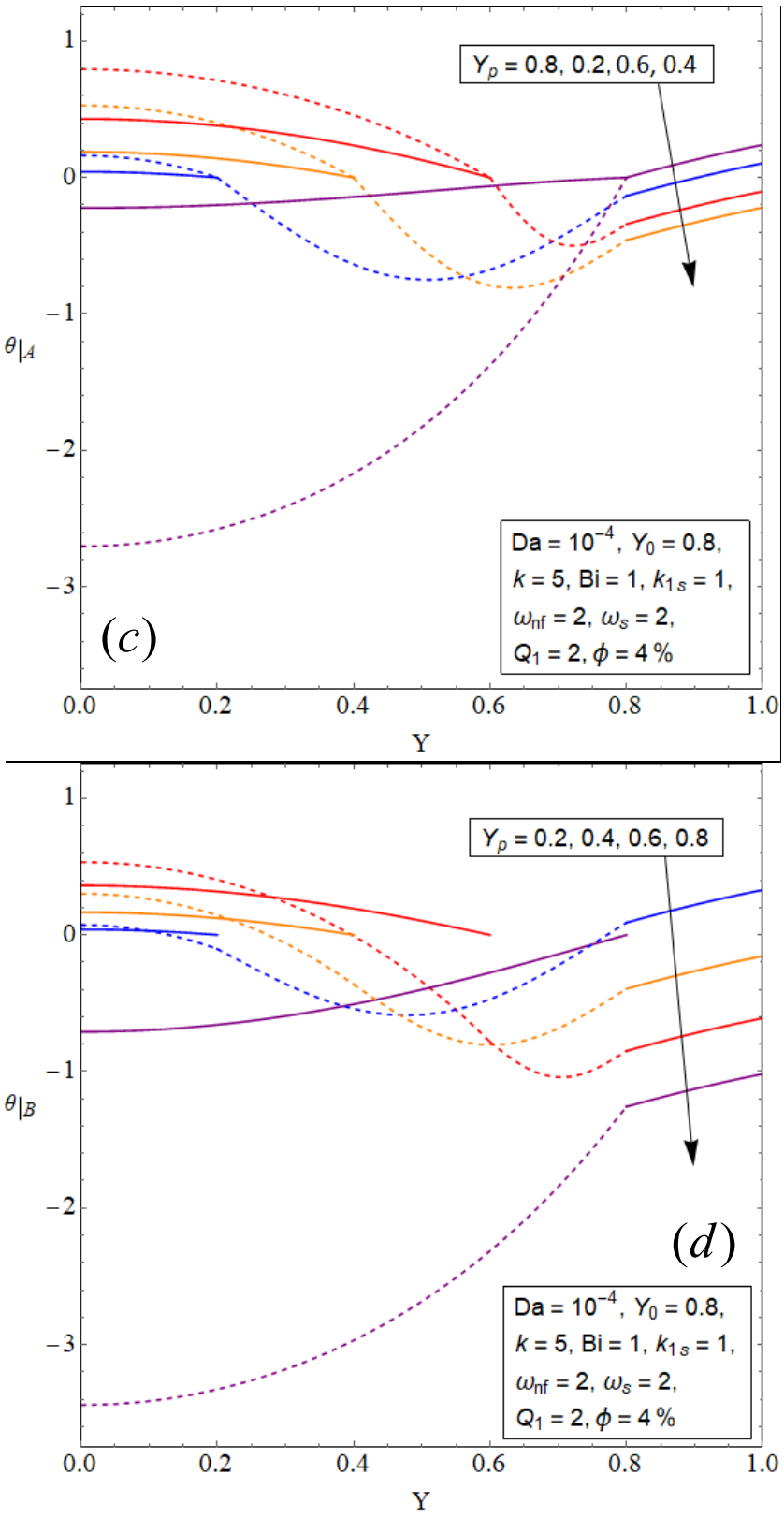

Fig. 3. Dimensionless temperature variation for various values of (*a*,*b*) thickness of the walls and (*c*,*d*) thickness for the porous material for Models A and B.

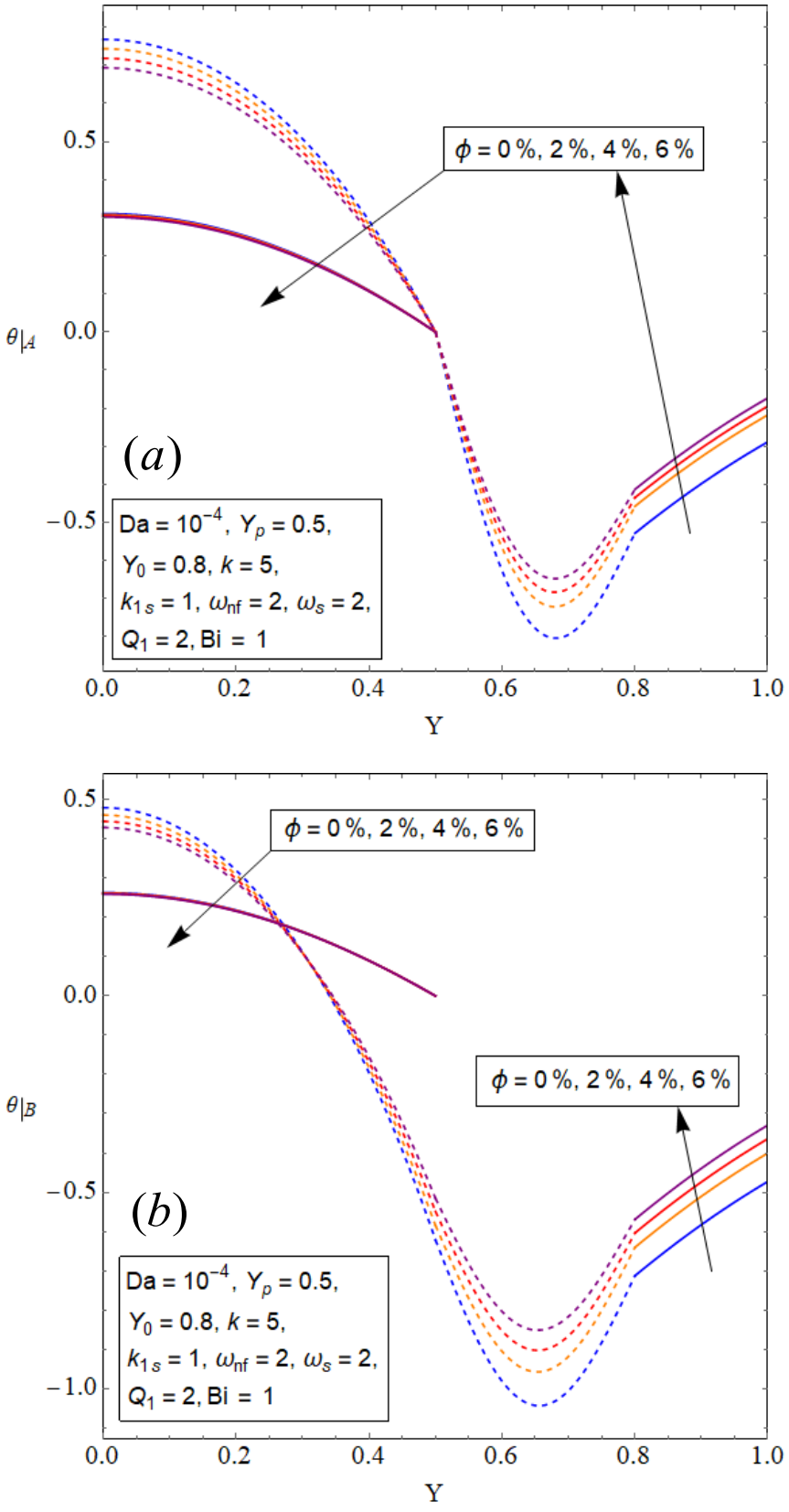

Fig. 4. Dimensionless temperature variation for various values of nanoparticles volumetric concentration for Models A and B.

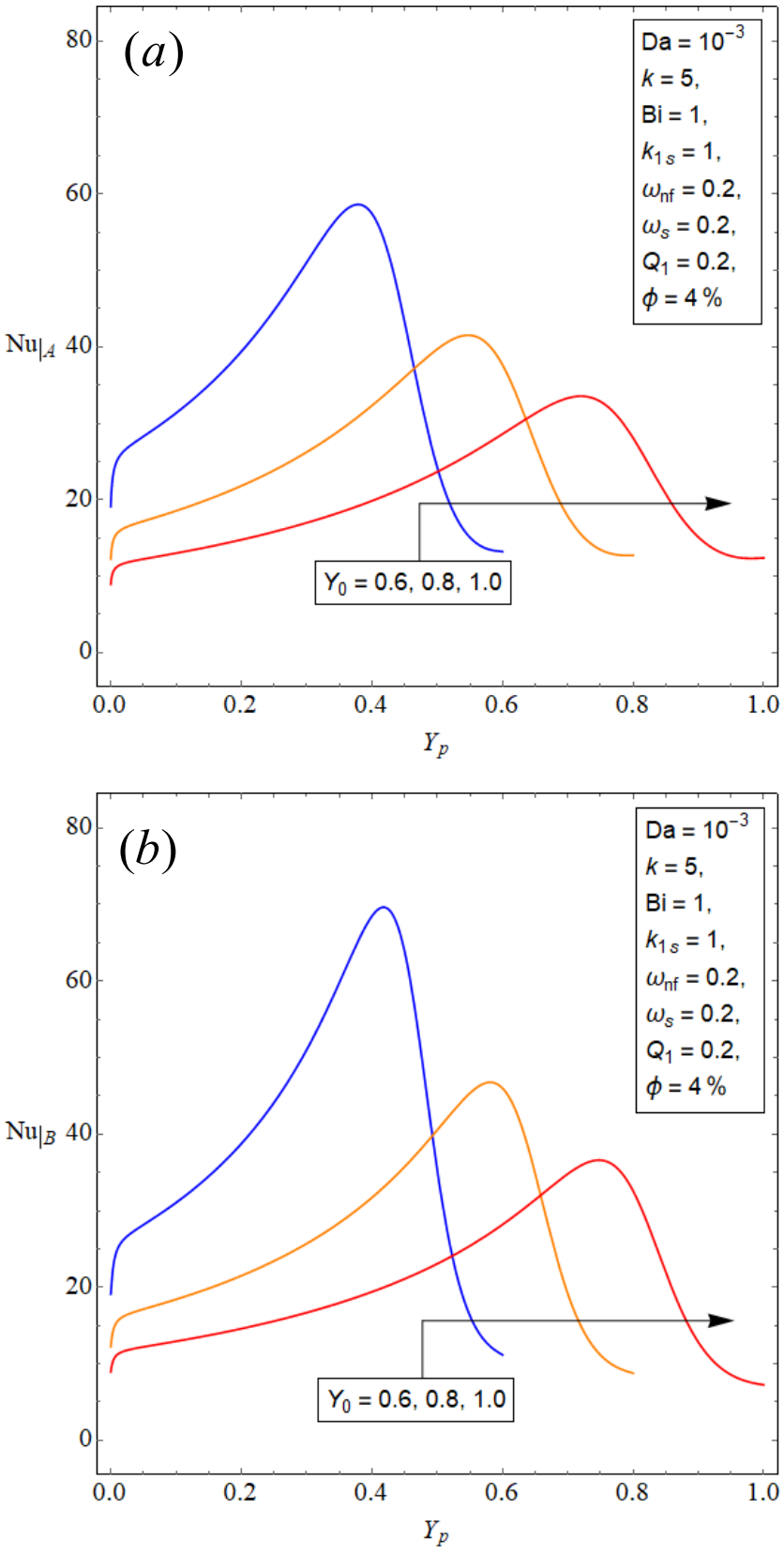

Fig. 5. Nusselt number verses thickness of the porous insert for various values of the walls' thickness for Models A and B.

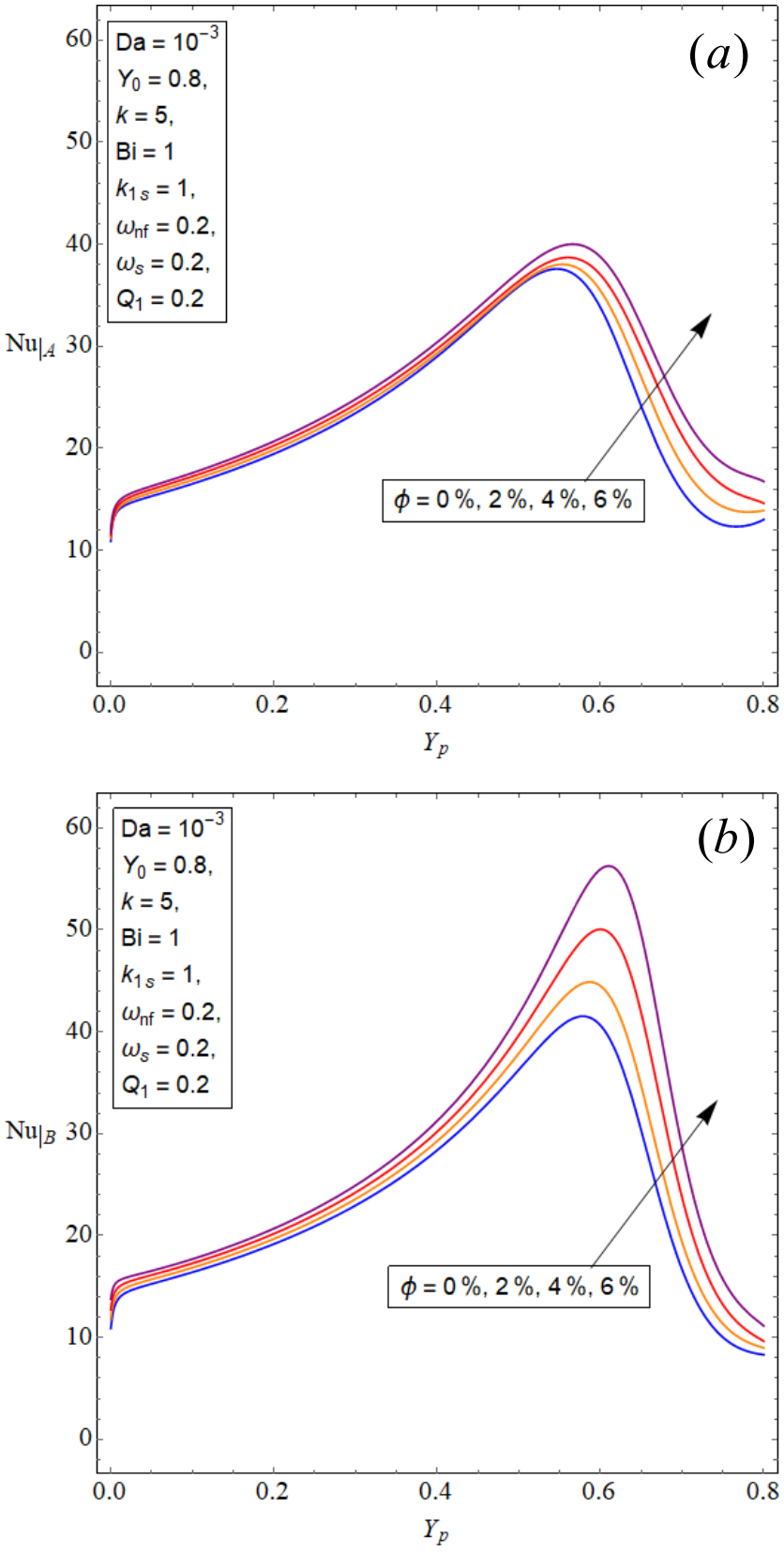

Fig. 6. Nusselt number verses thickness of the porous insert for various values of nanoparticles volumetric concentration for Models A and B.

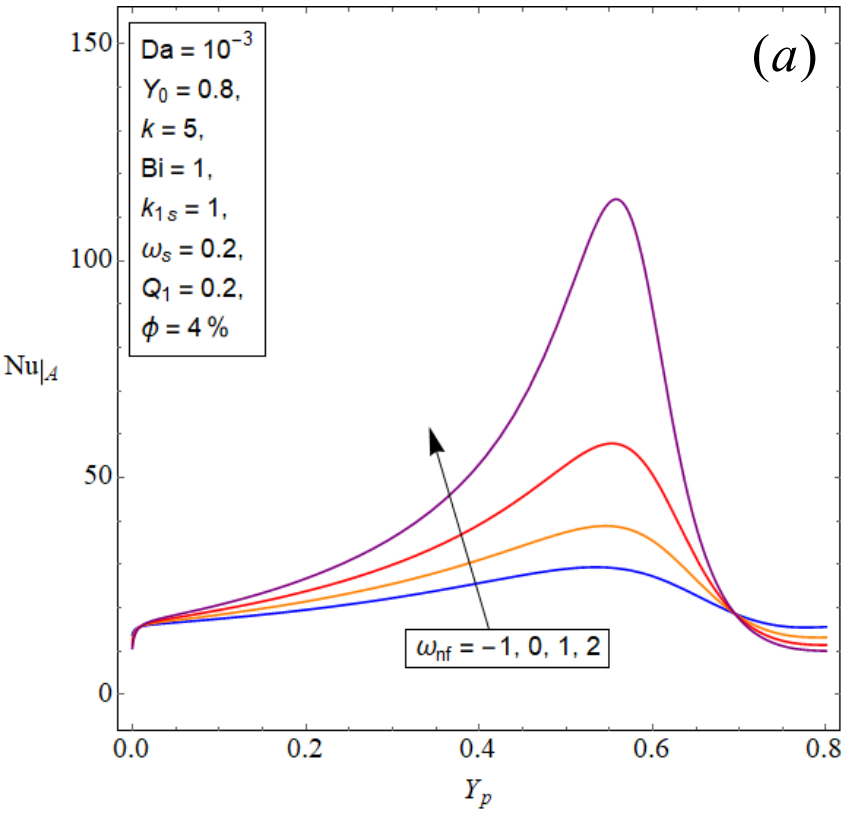
(a)
Da = 10^−3
Y0 = 0.8,
k = 5,
Bi = 1,
k1s = 1,
ωs = 0.2,
Q1 = 0.2,
ϕ = 4 %
ωnf = −1, 0, 1, 2
Nu|A
Yp
150
100
50
0
0.0
0.2
0.4
0.6
0.8

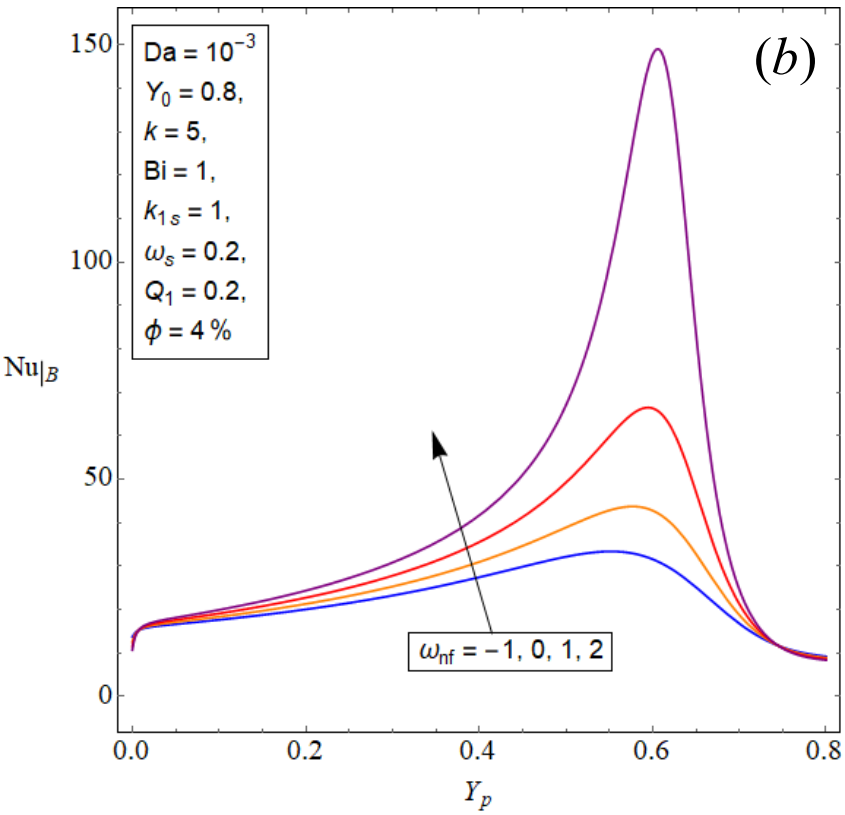
(b)
Da = 10^−3
Y0 = 0.8,
k = 5,
Bi = 1,
k1s = 1,
ωs = 0.2,
Q1 = 0.2,
ϕ = 4 %
ωnf = −1, 0, 1, 2
Nu|B
Yp
150
100
50
0
0.0
0.2
0.4
0.6
0.8

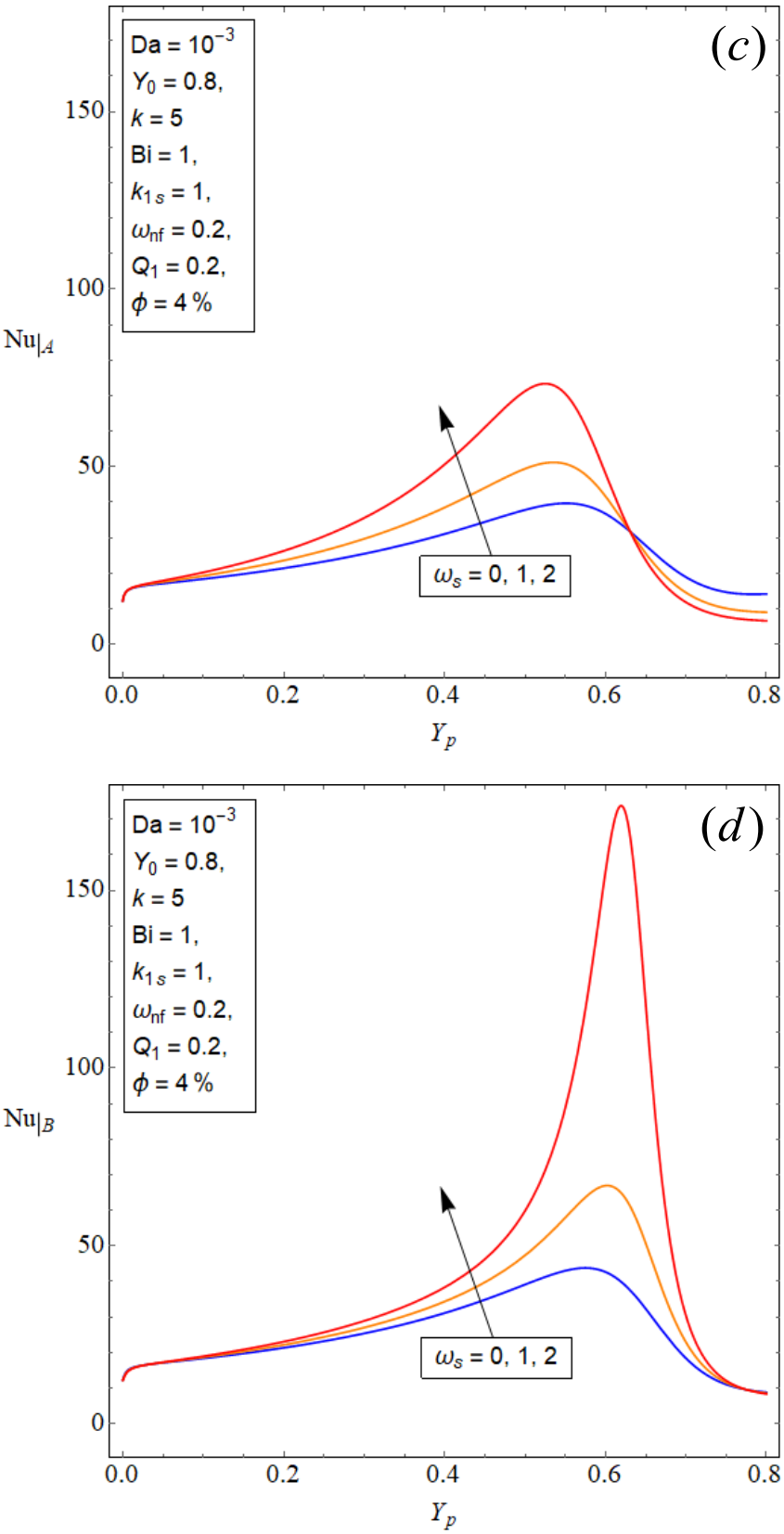

Fig. 7. Nusselt number verses thickness of the porous insert for various values of internal heat generation in (*a*,*b*) nanofluid and (*c*,*d*) solid phase of the porous section for Models A and B.

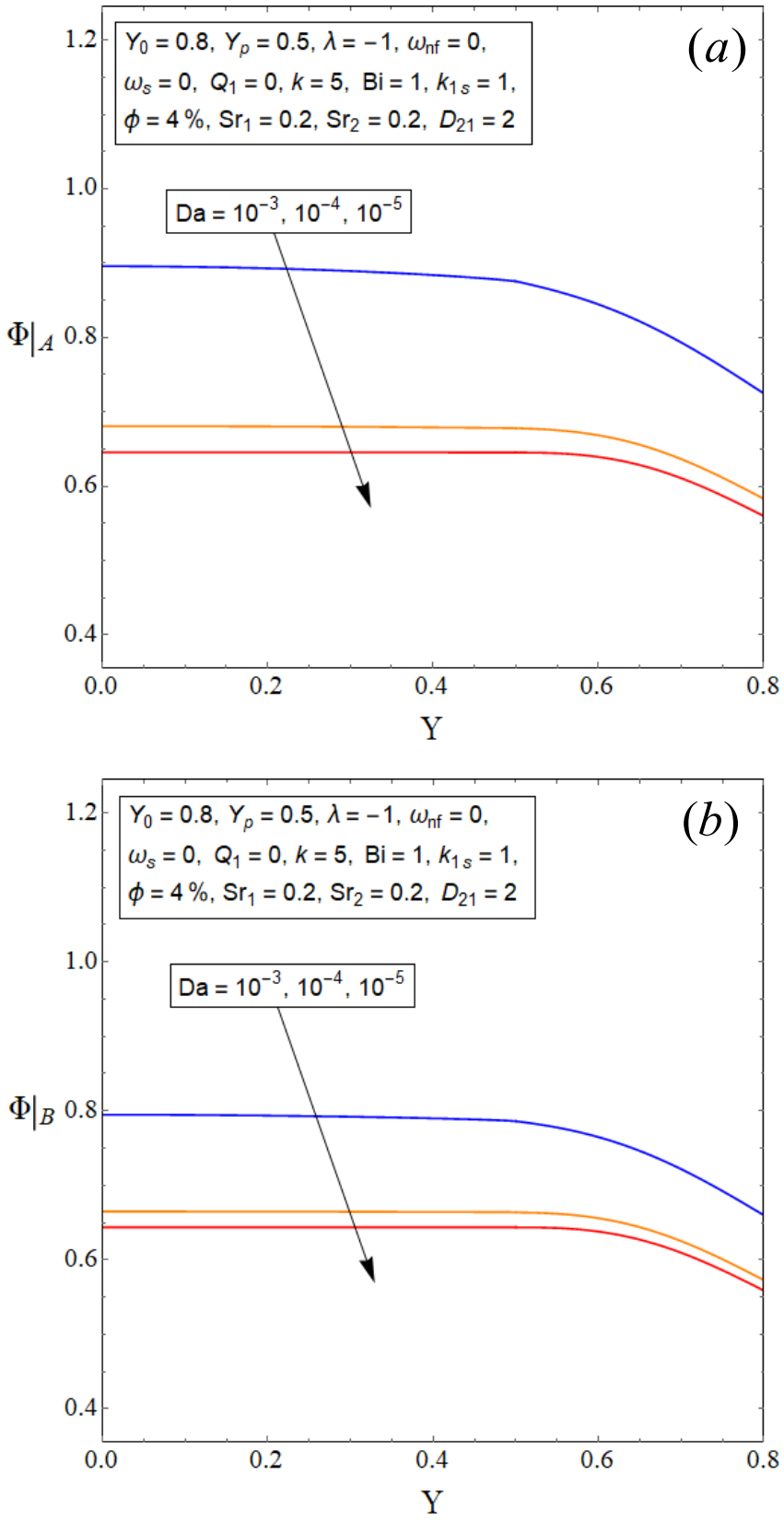

Fig. 8. Dimensionless concentration profiles for various values of Darcy number for Models A and B.

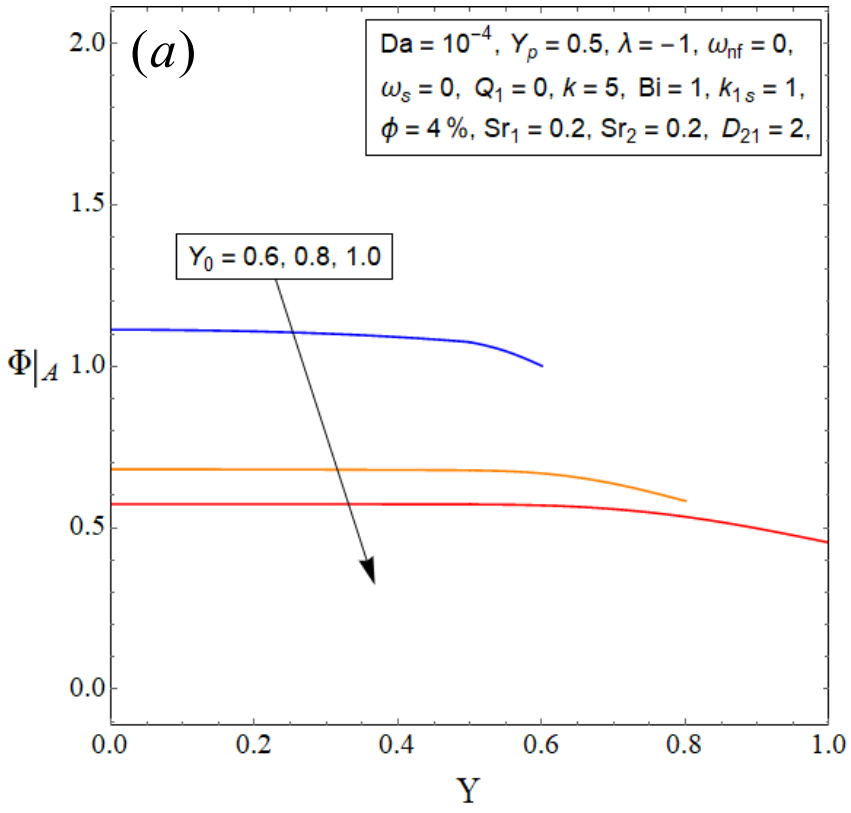
(a)
Da = 10^−4, Y_p = 0.5, λ = −1, ω_nf = 0,
ω_s = 0, Q_1 = 0, k = 5, Bi = 1, k_1s = 1,
ϕ = 4 %, Sr_1 = 0.2, Sr_2 = 0.2, D_21 = 2,
Y_0 = 0.6, 0.8, 1.0
Φ|_A
2.0
1.5
1.0
0.5
0.0
0.0
0.2
0.4
0.6
0.8
1.0
Y

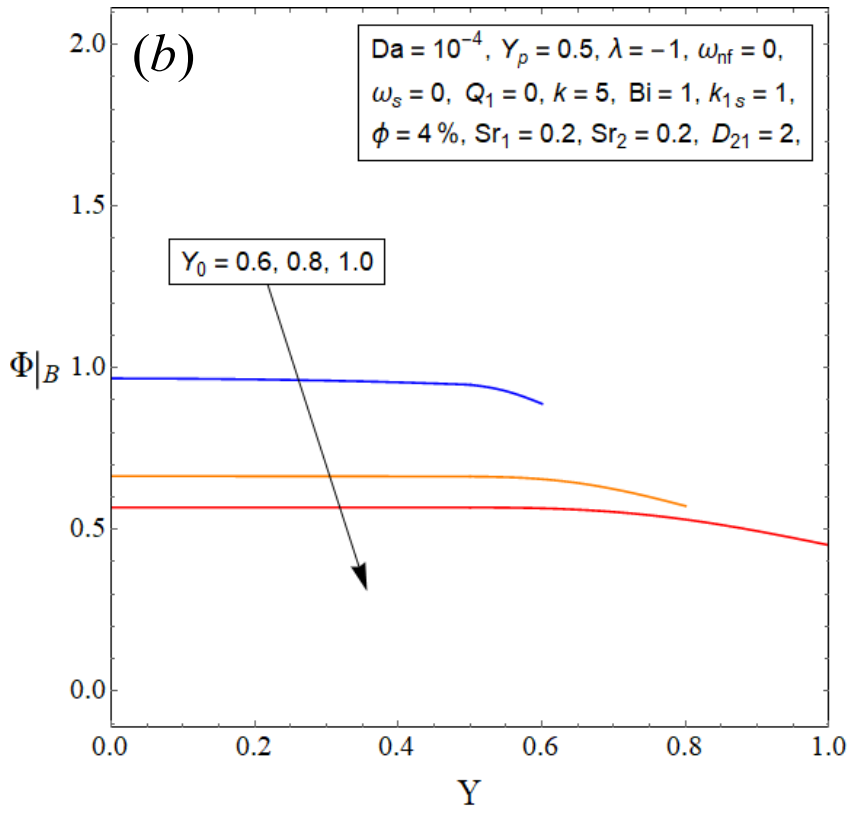
(b)
Da = 10^−4, Y_p = 0.5, λ = −1, ω_nf = 0,
ω_s = 0, Q_1 = 0, k = 5, Bi = 1, k_1s = 1,
ϕ = 4 %, Sr_1 = 0.2, Sr_2 = 0.2, D_21 = 2,
Y_0 = 0.6, 0.8, 1.0
Φ|_B
2.0
1.5
1.0
0.5
0.0
0.0
0.2
0.4
0.6
0.8
1.0
Y

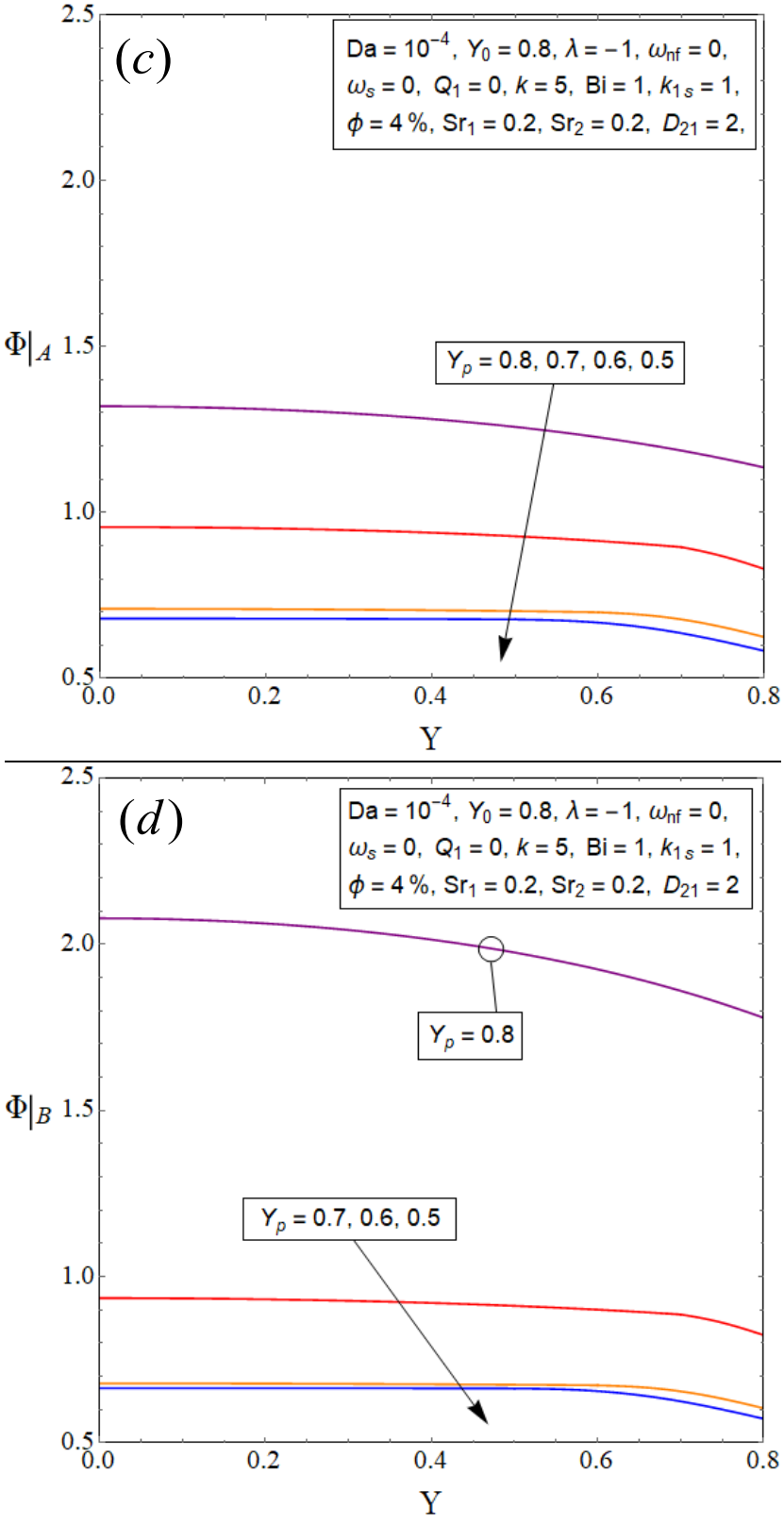

Fig. 9. Dimensionless concentration profiles for various values of (*a*,*b*) walls' thickness and (*c*,*d*) thickness of the porous insert for Models A and B.

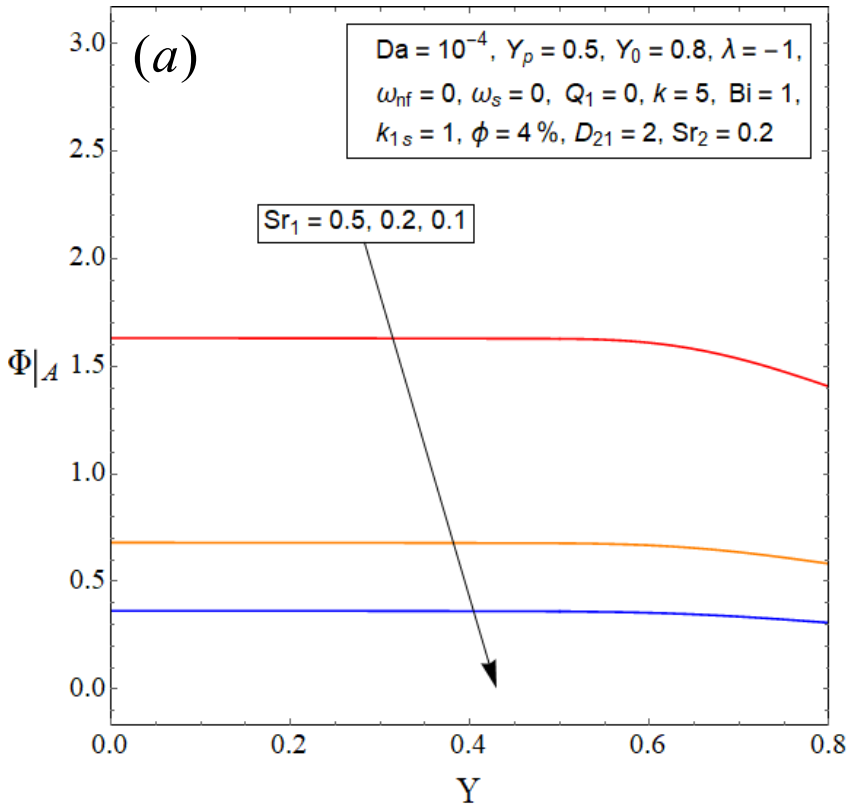
(a)
Da = 10^−4, Y_p = 0.5, Y_0 = 0.8, λ = −1,
ω_nf = 0, ω_s = 0, Q_1 = 0, k = 5, Bi = 1,
k_1s = 1, ϕ = 4 %, D_21 = 2, Sr_2 = 0.2
Sr_1 = 0.5, 0.2, 0.1
Φ|_A
Y
3.0
2.5
2.0
1.5
1.0
0.5
0.0
0.0
0.2
0.4
0.6
0.8

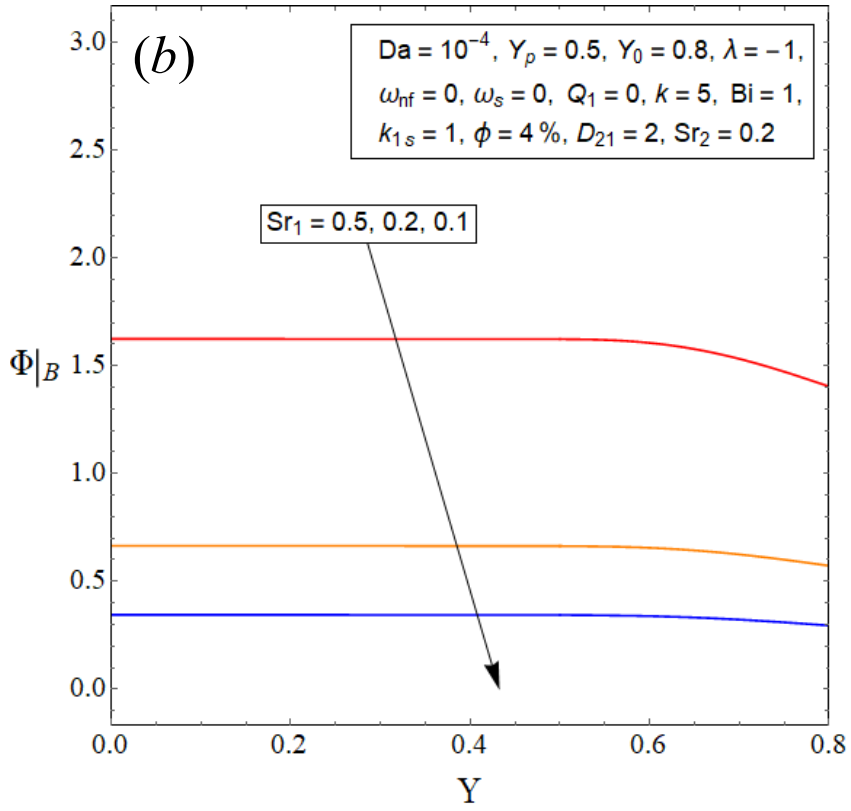
(b)
Da = 10^−4, Y_p = 0.5, Y_0 = 0.8, λ = −1,
ω_nf = 0, ω_s = 0, Q_1 = 0, k = 5, Bi = 1,
k_1s = 1, ϕ = 4 %, D_21 = 2, Sr_2 = 0.2
Sr_1 = 0.5, 0.2, 0.1
Φ|_B
Y
3.0
2.5
2.0
1.5
1.0
0.5
0.0
0.0
0.2
0.4
0.6
0.8

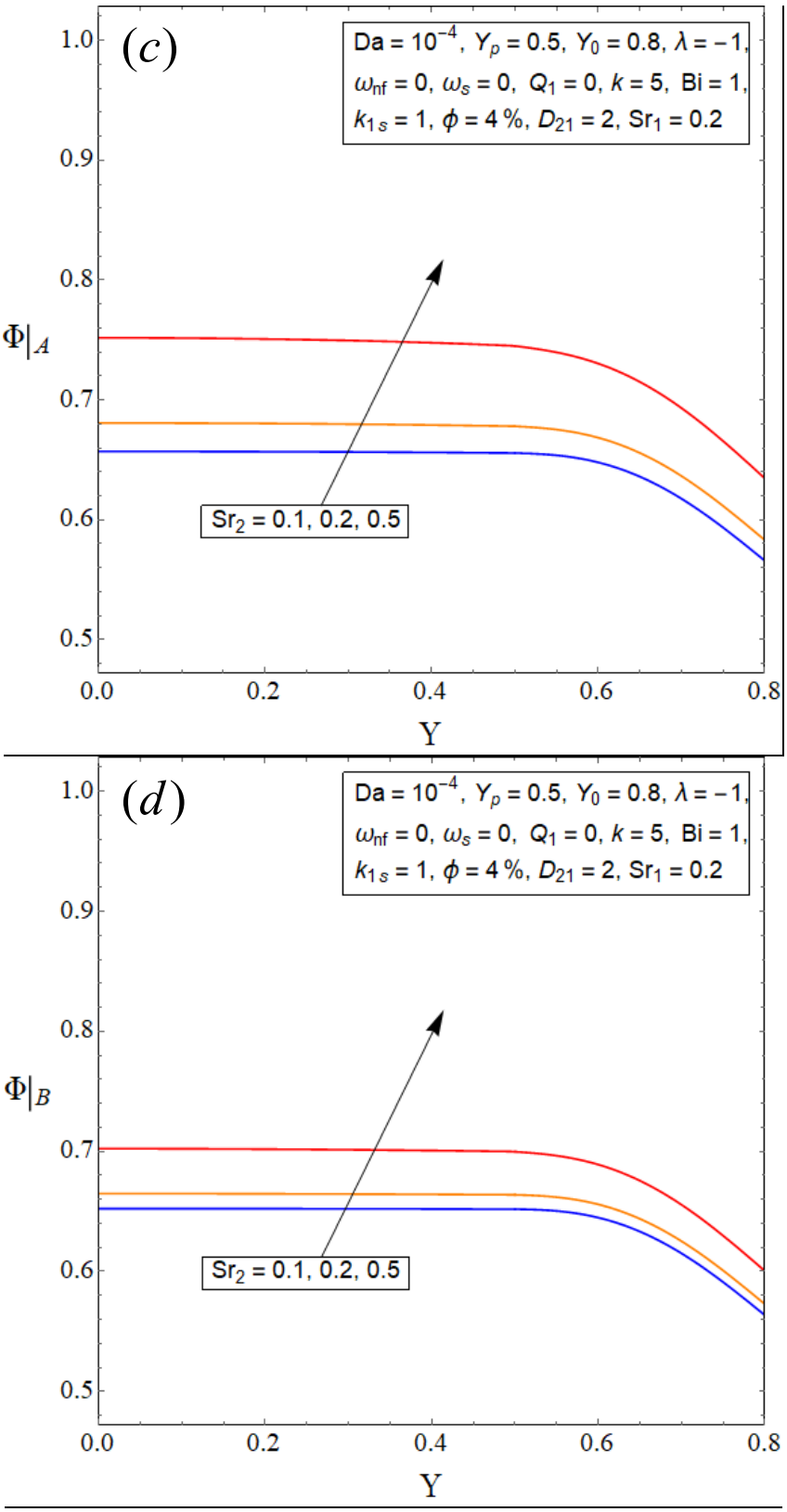

Fig. 10. Dimensionless concentration profiles for various values of (*a*, *b*) clear section Soret number and (*c*, *d*) porous section Soret number for Models A and B.

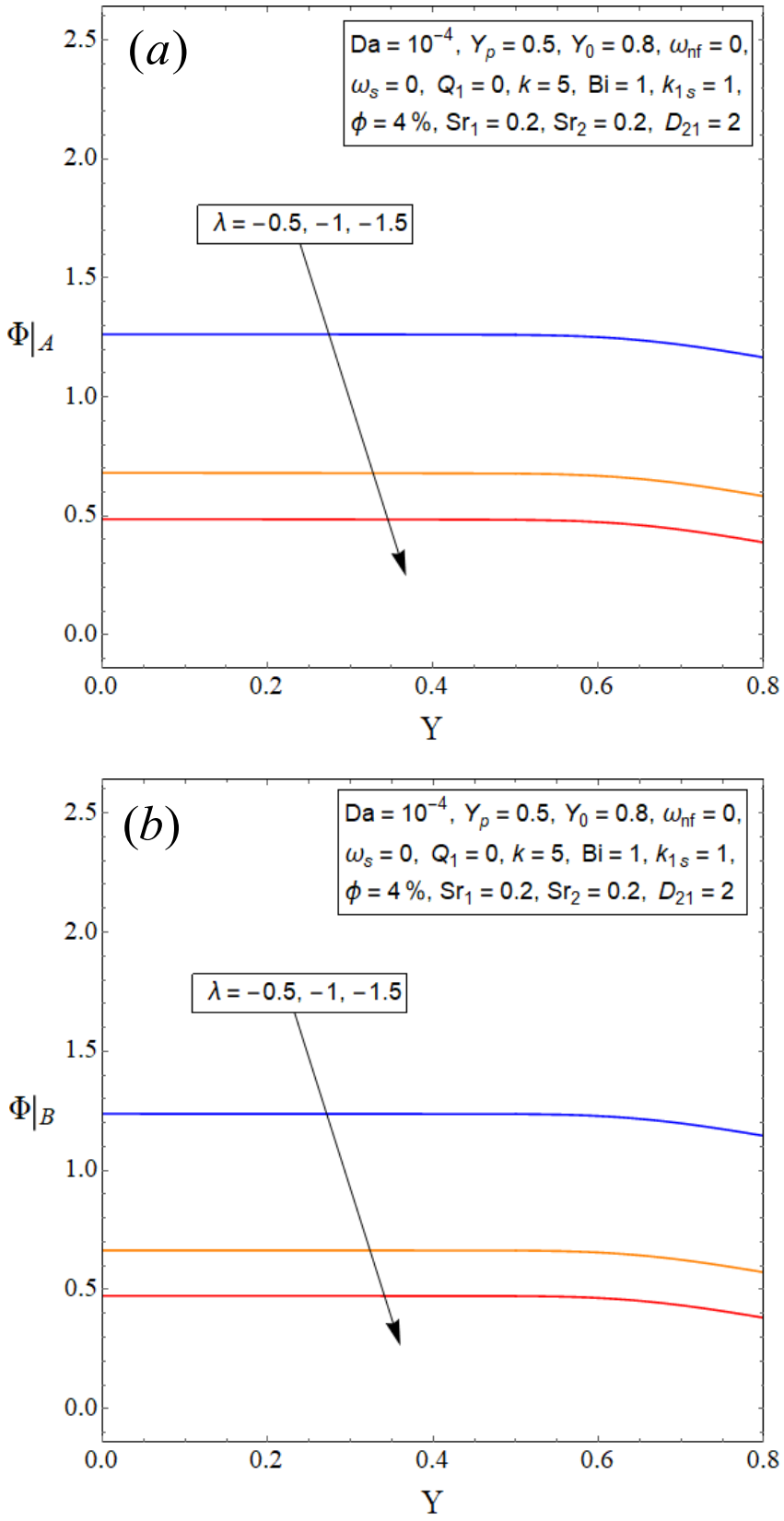

Fig. 11. Dimensionless concentration profiles for various values of Damköhler number for Models A and B.

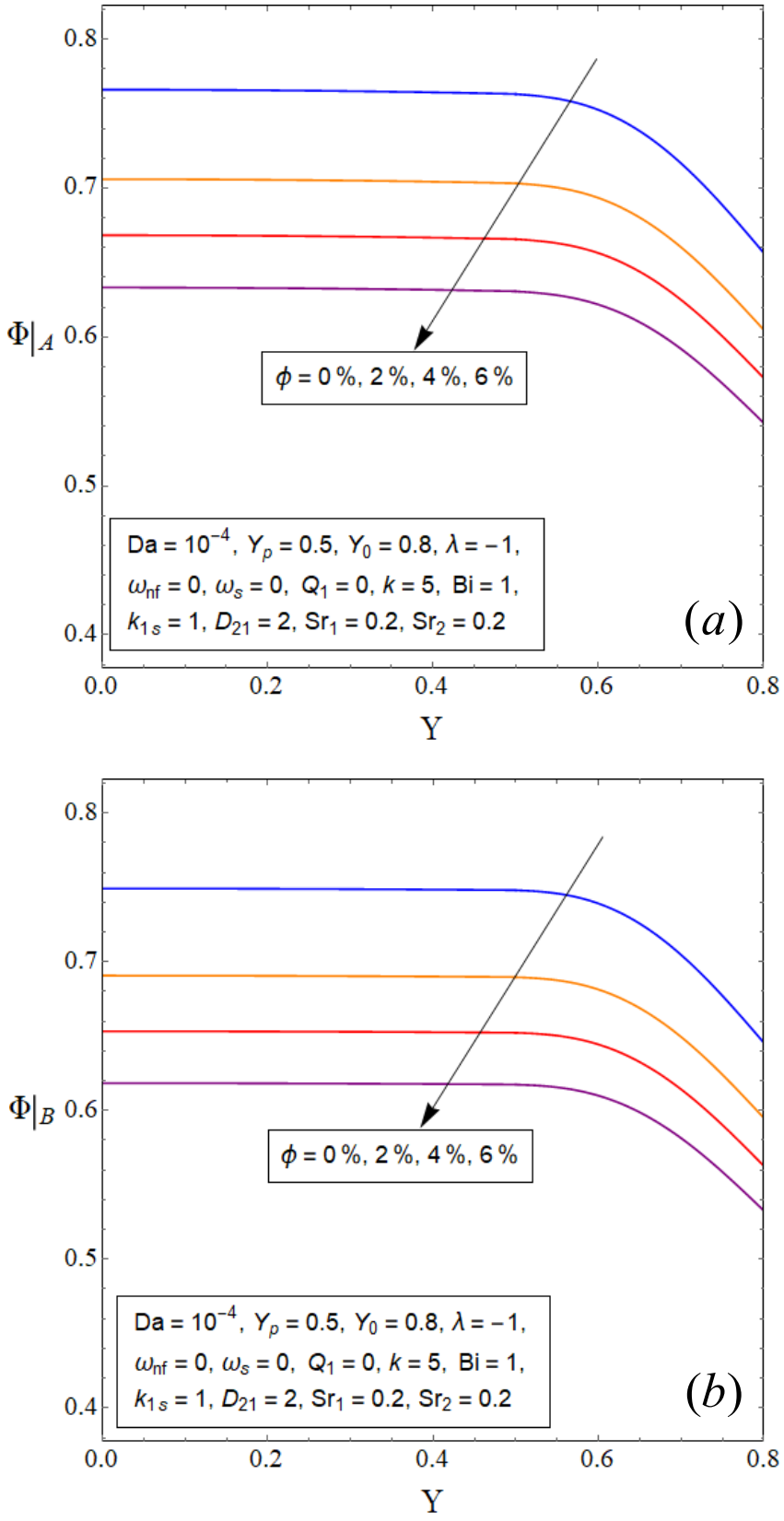

Fig. 12. Dimensionless species concentration profiles for various values of nanoparticles volumetric concentration for Models A and B.